

CANCER

The STEMRI trial: Magnetic resonance spectroscopy imaging can define tumor areas enriched in glioblastoma stem-like cells

Anthony Lemarié^{1,2*}, Vincent Lubrano^{3,4†}, Caroline Delmas^{1,5}, Amélie Lusque⁶, Juan-Pablo Cerapio¹, Marion Perrier¹, Aurore Siegfried^{1,7}, Florent Arnauduc^{1,2}, Yvan Nicaise^{1,2}, Perrine Dahan¹, Thomas Filleron⁶, Muriel Mounier⁸, Christine Toulas^{1,9}, Elizabeth Cohen-Jonathan Moyal^{1,2,10*}

Copyright © 2023 The Authors, some rights reserved; exclusive licensee American Association for the Advancement of Science. No claim to original U.S. Government Works. Distributed under a Creative Commons Attribution NonCommercial License 4.0 (CC BY-NC).

Despite maximally safe resection of the magnetic resonance imaging (MRI)-defined contrast-enhanced (CE) central tumor area and chemoradiotherapy, most patients with glioblastoma (GBM) relapse within a year in peritumoral FLAIR regions. Magnetic resonance spectroscopy imaging (MRSI) can discriminate metabolic tumor areas with higher recurrence potential as CNI+ regions (choline/*N*-acetyl-aspartate index >2) can predict relapse sites. As relapses are mainly imputed to glioblastoma stem-like cells (GSCs), CNI+ areas might be GSC enriched. In this prospective trial, 16 patients with GBM underwent MRSI/MRI before surgery/chemoradiotherapy to investigate GSC content in CNI-/+ biopsies from CE/FLAIR. Biopsy and derived-GSC characterization revealed a FLAIR/CNI+ sample enrichment in GSC and in gene signatures related to stemness, DNA repair, adhesion/migration, and mitochondrial bioenergetics. FLAIR/CNI+ samples generate GSC-enriched neurospheres faster than FLAIR/CNI-. Parameters assessing biopsy GSC content and time-to-neurosphere formation in FLAIR/CNI+ were associated with worse patient outcome. Preoperative MRI/MRSI would certainly allow better resection and targeting of FLAIR/CNI+ areas, as their GSC enrichment can predict worse outcomes.

INTRODUCTION

Glioblastoma (GBM, grade IV glioma) is the most frequent and aggressive malignant primary adult brain cancer. Surgical resection followed by chemo-radiotherapy (RT) [30 days of 2-Gy radiation and temozolomide (TMZ)] is the current standard of care. However, prognosis remains extremely poor, with a median survival of 15 to 16 months (1, 2). Recently, the adjunction of tumor treating fields to maintenance TMZ after chemo-RT was approved in several countries for newly diagnosed GBM, as this adjuvant treatment was shown in a phase 3 trial to increase median progression-free survival (PFS) to 6.7 months and median overall survival (OS) to 20.9 months (2). Recurrences may be notably explained by the major cellular heterogeneity of these tumors that contain GBM stem-like cells (GSCs) (3). These cells, rather than a specific single subpopulation within the tumor mass, should be more accurately defined by the fact they belong to a stem-cell state, mostly characterized by an unlimited self-renewal ability, an increased

tumorigenic potential associated with an intrinsic plasticity (4). Besides, GSC can be characterized by the overexpression of one or more stem markers [e.g., Sox2 (5), CD133 (6), Nestin (7), Olig2 (8), A2B5 (9), and integrin $\alpha 6$ (*ITGA6*) (10)], an important invasion capacity, their localization in perivascular niches, and a strong chemo/radioresistance (3, 11). Consequently, GSC targeting is a major therapeutic challenge in GBM management.

The tumor heterogeneity can be visualized and mapped by multimodal imaging including multimodal magnetic resonance imaging (MRI). MRI is a noninvasive instrument that is capable of producing high resolution (submillimetric) images of the brain using the phenomenon of proton spin resonance. This instrument is sensitive to many physical properties such as spin relaxometry (T1, T2, and T2*), spin interactions, spin density, or spin displacement. By measuring these properties, a lot of information about the microenvironment can be extracted such as the water/protein/lipid content, the blood flow/volume, the cell density/shape/size, tissue texture, or the content of paramagnetic contrast agent. In these MRI images, GBM are clearly shown as heterogeneous tissues (12). The typical imaging features of a GBM include an infiltrative, heterogeneous, and ring-enhancing lesion with central necrosis and surrounding peritumoral edema. In clinical routine, two main sequences are commonly used to image GBM: a contrast-enhanced (CE) T1-weighted image (CE-T1W) that reveals, with gadolinium enhancement, the active regions that present blood-brain barrier breakdown (usually a hyperintense rim with a necrotic core) and a T2-weighted and fluid-attenuated inversion recovery (T2W/FLAIR) image that highlights other tissue abnormalities in the peritumoral region (e.g., tissue softening, water infiltration, and vasogenic edema) (12).

¹CRCT, Université de Toulouse, Inserm, CNRS, Université Toulouse III–Paul Sabatier, Centre de Recherches en Cancérologie de Toulouse, Toulouse, France. ²UFR Santé, Université de Toulouse III–Paul Sabatier, Toulouse, France. ³TONIC, Université de Toulouse, Inserm, CNRS, Université Toulouse III–Paul Sabatier, Toulouse Neuro Imaging Center, Toulouse, France. ⁴CHU de Toulouse, Neurosurgery Department, Toulouse, France. ⁵Institut Claudius Regaud, IUCT-Oncopole, Interface Department, Toulouse, France. ⁶Institut Claudius Regaud, IUCT-Oncopole, Biostatistics and Health Data Science Unit, Toulouse, France. ⁷CHU de Toulouse, Anatomopathology Department, Toulouse, France. ⁸Institut Claudius Regaud, IUCT-Oncopole, Clinical Trials Office, Toulouse, France. ⁹Institut Claudius Regaud, IUCT-Oncopole, Cancer Biology Department, Molecular Oncology Division, Toulouse, France. ¹⁰Institut Claudius Regaud, IUCT-Oncopole, Radiation Oncology Department, Toulouse, France.

*Corresponding author. Email: anthony.lemarie@inserm.fr (A.Le.); moyal.elizabeth@iuct-oncopole.fr (E.C.-J.M.)

†Present address: Clinique de l'Union, Neurosurgery Department, Saint Jean, France.

Beside anatomic and functional sequences, *in vivo* proton (^1H) magnetic-resonance spectroscopic imaging (MRSI), which allows to study metabolic heterogeneity (13), has shown convincing and promising results in GBM related to tumor grade and delimitation, prediction of resistance patterns, and patient prognosis (14–21). MRSI measures the spatial distribution and concentration of tissue metabolites like choline (Cho) and *N*-acetyl-aspartate (NAA), which are respectively membrane and neuronal markers, as well as, among others, lactate (necrosis and anaerobic metabolism), creatine/phosphocreatine (adenosine triphosphate metabolism), or myoinositol (putative astroglial marker). An elevated Cho/NAA index (CNI) indicates increased membrane turnover (i.e., cellular proliferation) and reduced neuron density and is considered to highlight a metabolically active zone of the tumor in high-grade gliomas (22, 23). This metabolic ratio, notably when the CNI is greater than 2 (CNI+), is an interesting predictor of GBM patient survival (17–19) and recurrence location (16, 22). Our previous works demonstrated that MRSI is useful in identifying tumor areas with a higher potential for recurrence (14, 15). In our first study (14), we performed the follow-up by MRI and MRSI of nine patients included in a phase 1 trial associating tipifarnib and RT for GBM primary treatment (24) and observed in pre-RT data that CNI+ regions accounted for 25% of CE regions (in CE-T1W sequence) and 10% of regions of T2W/FLAIR hyperintensity

corresponding to the infiltrative areas. We showed that the presence of metabolically active CNI+ regions was predictive of the site of relapse after RT, both in CE and FLAIR areas (14). Cho/NAA ratio was also described by other teams as a parameter that may predict earlier GBM recurrence (20), shorter PFS and OS (18), localization of invasive margin of GBM (25), but also treatment failure for antiangiogenic combined therapy (21).

Considering that pre-RT CNI+ GBM areas are predictive of the recurrence zones after treatment (14) and that GSC were demonstrated to mediate recurrence after chemo-RT (26, 27), we hypothesized that these particular metabolic regions (i.e., CNI+) may be enriched in GSC and by this way could favor tumor relapse in these zones. In this regard, recent works highlighted that higher-CNI tumor areas were correlated with stronger Sox2 immunostaining in GBM (28). In addition, the MRSI data obtained from tumors generated in mice brain after xenograft of patient-derived GSC unveiled a notable increase in Cho (or Chol-containing compounds) and decrease in NAA (29, 30). Together, a noticeable correlation between CNI+ areas and GSC enrichment might be suspected. To answer to this hypothesis, we designed and performed the STEMRI trial (NCT01872221) aiming to study by MRI-MRSI-guided resection the potential enrichment of the CNI+ regions with GSC in comparison with CNI– tumor regions. This trial, whose flow diagram is shown in Fig. 1, was designed to fully characterize and

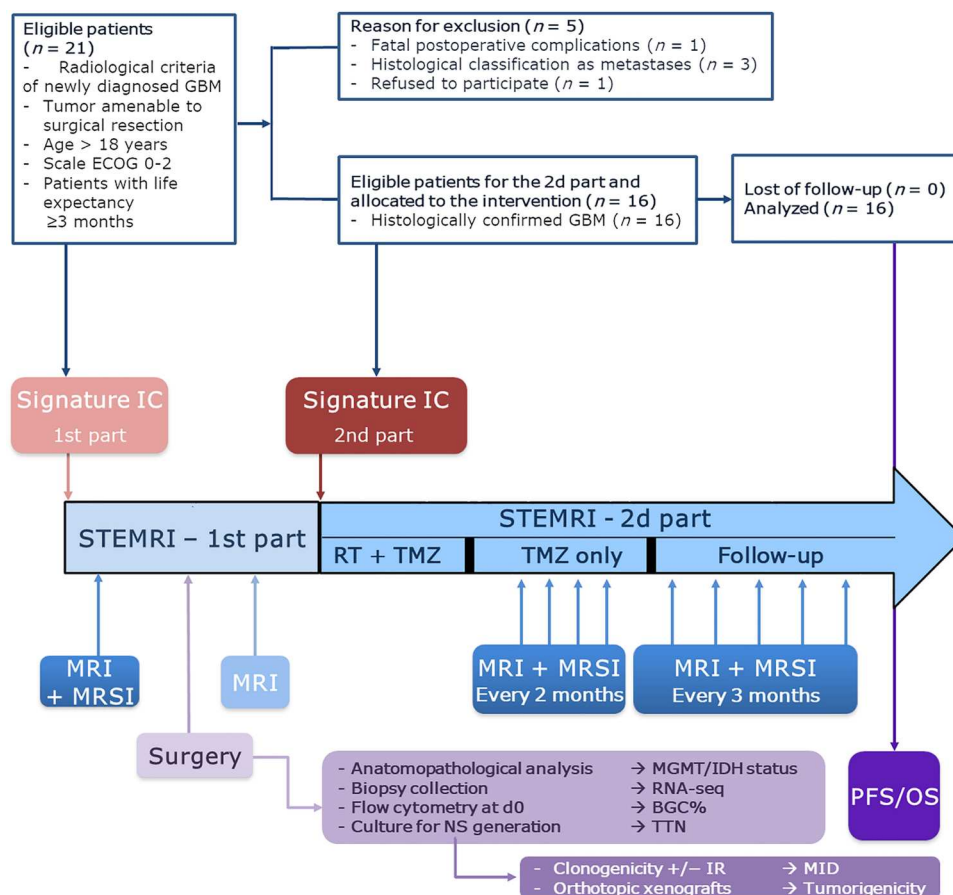


Fig. 1. STEMRI trial flow diagram. IC, informed consents; *IDH*, isocitrate dehydrogenase; NS, neurosphere; BGC%, biopsy GSC content percentage; TTN, time-to-neurosphere formation; MID, mean inactivation dose.

compare these CNI-/+ regions in both CE and FLAIR zones and then to correlate these data with patients' clinical outcome after standard chemo-RT treatment.

RESULTS

Patient's characteristics and clinical outcome

According to inclusion criteria, 21 patients were enrolled in the first part of the study. However, five patients could not be included in the second part because of inclusion and exclusion criteria. Three patients were diagnosed after histological analysis as pulmonary, renal, and melanoma brain metastases, respectively. One patient experienced postoperative complications that resulted in his death. One patient has decided to withdraw from the trial after surgery to receive chemo-RT sessions in a different hospital center. As a consequence, 16 patients were included in the second part of the trial and evaluable for the entire study. The patient's characteristics are provided in Table 1 and table S1. Their age ranged between 37 and 78, with a median age of 64 years, 5 women and 11 men. Notably, 43.7% of the patients had a temporal tumor, and percentages for parietal and frontal areas were 18.7 and 37.5%, respectively. All patients had a GBM, according to 2021 World Health Organization classification (*IDH1/2* wild type) (31). A total of 68.75% were shown to have an unmethylated *MGMT* (*O*⁶-methylguanine-DNA methyltransferase) promoter and 31.25% a methylated *MGMT*. All the 16 patients received a cumulative irradiation (IR) dose of 60 Gy and concomitant TMZ. At the end of the trial, all the 16 patients experienced GBM progression, corresponding to

either clinical tumor progression ($n = 12$) or death event ($n = 4$), and all 16 patients had died. PFS and OS were shown for each patient in fig. S1. Median PFS and OS were respectively estimated to 6.5 months [95% confidence interval (CI): 5.5 to 12.5] and 20.1 months (95% CI: 12.7 to 25.7). Univariate analysis of OS and PFS according to main clinical variables such as age of inclusion, patient sex, preoperative performance scale ECOG (established by the Eastern Cooperative Oncology Group), and *MGMT* methylation status was then performed. These analyses highlighted a significant association between *MGMT* promoter methylation and an increased PFS ($P = 0.0226$) and OS ($P = 0.0213$) (table S2, A and B).

Patient biopsies

All the 16 patients had different tumor biopsies performed according to the study for analysis and for generation of derived GSC-enriched neurospheres (NS). For each patient, four samples, when possible, were biopsied in four different tumor areas: FLAIR/CNI- (group 1), FLAIR/CNI+ (group 2), CE/CNI- (group 3), CE/CNI+ (group 4), as described in Fig. 2 (A and B) and in Materials and Methods. The details of the biopsies per patient are shown in Table 2 and table S3. To summarize, 54 biopsy samples were collected for 16 patients and processed within 24 hours after surgical resection (Table 1 and table S1). These biopsies samples were divided immediately after surgery in three parts for (i) RNA extraction [51 of 54 biopsies generated optimal-quality RNA for RNA sequencing (RNA-seq)], (ii) fluorescence-activated cell sorting (FACS) analysis of the pool of GSC at day 0 (54 of 54), and (iii) long-term culture in stem cell

Table 1. Patients' main characteristics. The full table can be found in the Supplementary Materials as table S1. IR, irradiation; WT, wild type.

Patient number	Tumor name	Sex	Age range (years)	Treatment			Nature of the progression	PFS (months)	OS (months)	<i>MGMT</i> promoter methylation status (Y/N)	<i>IDH</i> status
				IR dose (Gy)	Concomitant TMZ dose (mg/m ²)	Adjuvant TMZ cycles					
Sub-001	SRA	M	76–80	60	3150	2	Progression	6.21	8.05	N	WT
Sub-002	SRB	F	76–80	60	3150	0	Progression	3.68	21.32	N	WT
Sub-003	SRC	M	66–70	60	3150	6	Progression	14.98	30.65	Y	WT
Sub-006	SRF	F	71–75	60	1950	0	Death (heart attack)	2.76	2.76	N	WT
Sub-007	SRG	M	56–60	60	3300	2	Progression	6.11	16.95	Y	WT
Sub-008	SRH	F	56–60	60	3150	6	Progression	21.16	36.6	Y	WT
Sub-009	SRI	F	71–75	60	3525	6	Progression	12.45	29.34	Y	WT
Sub-010	SRJ	M	51–55	60	3150	4	Death	15.11	20.4	N	WT
Sub-012	SRK	M	61–65	60	3150	5	Progression	9.1	27.27	N	WT
Sub-013	SRL	F	56–60	60	3225	1	Death	5.19	6.87	N	WT
Sub-014	SRM	M	71–75	60	3150	3	Progression	5.45	18.56	N	WT
Sub-015	SRN	M	71–75	60	3150	3	Progression	5.55	20.11	N	WT
Sub-017	SRO	M	46–50	60	2775	6	Progression	10.74	25.69	N	WT
Sub-019	SRQ	M	76–80	60	2775	0	Death (nocardiosis)	21.09	21.09	Y	WT
Sub-020	SRR	M	36–40	60	3525	3	Progression	6.47	14.26	N	WT
Sub-021	SRS	M	56–60	60	3150	5	Progression	8.67	12.68	N	WT

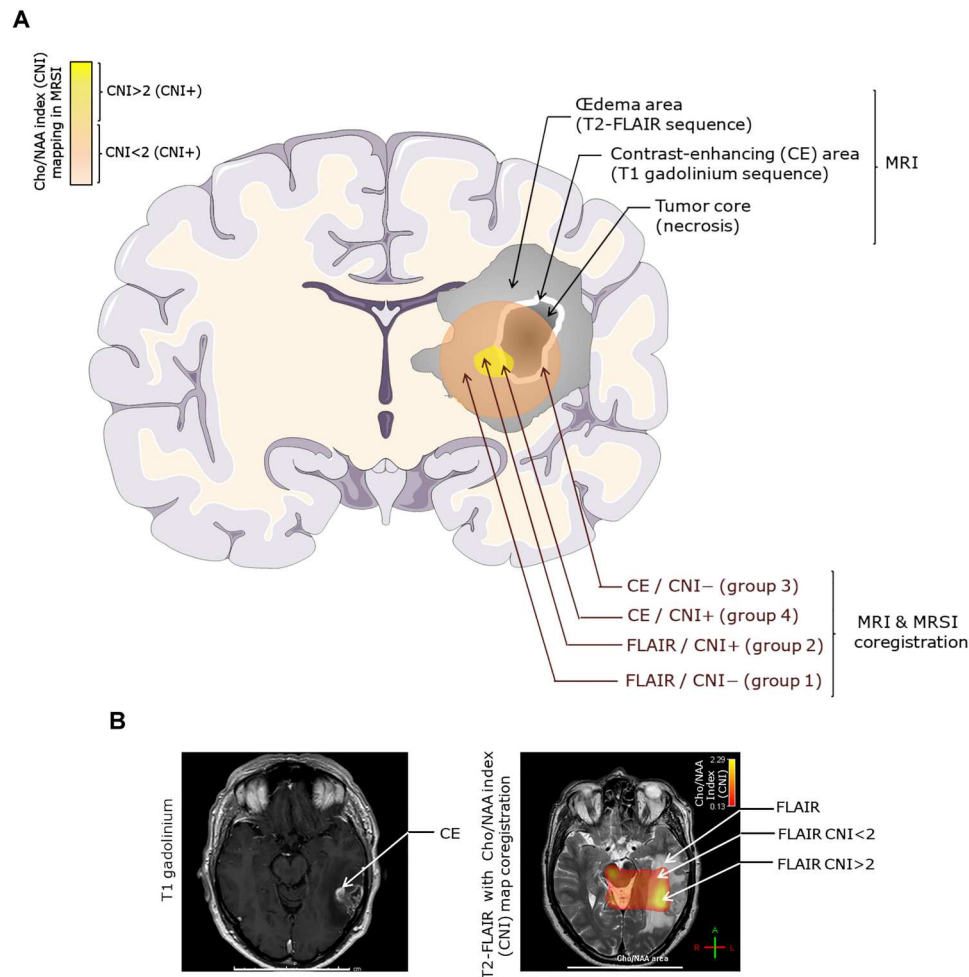


Fig. 2. STEMRI trial design. General descriptive scheme (A) and MRI/MRSI representative (Sub-003 patient) images (B) of the study strategy for surgical samples collection. Preoperative MRI/MRSI coregistration allowed the determination of two CNI metabolic zones (CNI < 2 and CNI > 2) in both CE and FLAIR areas, determined through T1 gadolinium and T2-FLAIR MRI sequences, respectively. A maximum of four different biopsies were then collected for each patient in the above described zones: FLAIR/CNI- (group 1), FLAIR/CNI+ (group 2), CE/CNI- (group 3), and CE/CNI+ (group 4). (B) Scale bar, 11 cm.

medium to generate NS enriched in GBM cells in a stem-like state (hereinafter referred to as GSC subpopulation). In these restrictive culture conditions, 42 of 54 processed biopsies led to stable primary-NS generation and, among them, 34 of 54 were able to generate secondary NS in culture (Table 2).

GSC quantification in patient's biopsies

We compared by FACS the percentages of the GSC subpopulation in each biopsy just after surgery (day 0) between FLAIR/CNI- and FLAIR/CNI+ as well as between CE/CNI- and CE/CNI+ tumor areas. For the 12 pairs of biopsies CNI-/CNI+ in the FLAIR area, the biopsy GSC content at D0 (BGC%) was significantly ($P = 0.0121$) higher in the CNI+ biopsies (Fig. 3A and table S4). However, no significant difference could be observed in the CE zone between CNI- and CNI+ biopsies (Fig. 3B and table S4). Beyond pairs, when all the samples were considered, we observed similar results between CNI- and CNI+ in FLAIR and CE areas, respectively (fig. S2A). Notably, when all biopsies of the CNI- and CNI+ were considered, regardless of their FLAIR or CE origin, the observed increase of BGC% in CNI+ appeared to be

not significant. On the contrary, if we compare CE (tumoral) and FLAIR (peritumoral) zones, regardless of their CNI status, a strong increase of the BGC% in CE biopsies can be highlighted (Fig. 3A). We also analyzed by FACS the expression of stem and differentiation markers in the GSC population in each biopsy. Only a nonsignificant increase in the stem markers CD44, CD15, and Nestin could be observed between CNI- and CNI+ in FLAIR, but no clear tendency between CNI- and CNI+ in CE zone (Fig. 3, C and D) or regardless of the FLAIR or CE origin (fig. S2B). However, CE biopsies, regardless of their CNI status, comprise GSC-overexpressing stem markers Nestin, CD44 (32), Sox2, and integrin $\beta 8$ (*ITGB8*) (11, 33), in comparison with GSC contained in FLAIR biopsies, which seem to overexpress the oligodendrocytic marker O4 (fig. S2B).

NS generation from patient's biopsies

According to FACS analysis of GSC content in biopsies, there is a notable inpatient heterogeneity in FLAIR tumor areas between CNI- and CNI+ zones. In this inflammatory and edematous peritumoral area, CNI+ biopsies appeared to be enriched in GSC

Table 2. Tumor samples' main characteristics. The full table can be found in the Supplementary Materials as table S3. nd, not determined; Ne, neural; Mes, Mesenchymal; PN, proneural; CI, classical.

Patient number	Tumorname	Tumor localization	Sex	Biopsies (Y/N)	Sample name	Biopsy GSC content (BGC) at day 0 (%)	Biopsy molecular classification		Stable primary-NS generation (Y/N)	Time to NS generation (days)	Stable secondary-NS generation (Y/N)
							Verhaak (34) PN Ne Mes CI	Wang (35) PN Mes CI			
Sub-001	SRA	(1) FLAIR/CNI-	M	N	-	-	-	-	-	-	-
		(2) FLAIR/CNI+		Y	SRA4	6.08	PN	PN	Y	13	Y
		(3) CE/CNI-		Y	SRA5	7.02	PN	PN	Y	8	Y
		(4) CE/CNI+		N	-	-	-	-	-	-	-
Sub-002	SRB	(1) FLAIR/CNI-	F	Y	SRB3	10.56	Ne	PN	Y	36	Y
		(2) FLAIR/CNI+		N	-	-	-	-	-	-	-
		(3) CE/CNI-		Y	SRB1	20.1	Mes	Mes	Y	50	Y
		(4) CE/CNI+		Y	SRB2	44.57	Mes	Mes	Y	11	Y
Sub-003	SRC	(1) FLAIR/CNI-	M	Y	SRC1	6	Ne	PN	Y	46	Y
		(2) FLAIR/CNI+		Y	SRC2	12.1	Ne	PN	Y	16	Y
		(3) CE/CNI-		Y	SRC3	40.15	Ne	CI	Y	16	Y
		(4) CE/CNI+		Y	SRC4	48.8	CI	PN	Y	53	Y
Sub-006	SRF	(1) FLAIR/CNI-	F	Y	SRF1	9.03	Ne	CI	N	-	N
		(2) FLAIR/CNI+		Y	SRF5	22.97	CI	CI	Y	11	N
		(3) CE/CNI-		Y	SRF3	4.78	Mes	Mes	N	-	N
		(4) CE/CNI+		Y	SRF4	9.22	PN	Mes	N	-	N
Sub-007	SRG	(1) FLAIR/CNI-	M	Y	SRG5	9.1	Ne	PN	Y	60	N
		(2) FLAIR/CNI+		Y	SRG4	10.8	Ne	Mes	Y	21	Y
		(3) CE/CNI-		Y	SRG1	39	Mes	Mes	Y	2	Y
		(4) CE/CNI+		Y	SRG2	22.7	Mes	Mes	Y	2	Y
Sub-008	SRH	(1) FLAIR/CNI-	F	Y	SRH1	4.39	Mes	CI	nd	nd	N
		(2) FLAIR/CNI+		Y	SRH3	2.52	CI	CI	Y	19	Y
		(3) CE/CNI-		Y	SRH2	16.49	CI	CI	Y	5	Y
		(4) CE/CNI+		Y	SRH4	10.18	nd	nd	N	-	N
Sub-009	SRI	(1) FLAIR/CNI-	F	N	-	-	-	-	-	-	-
		(2) FLAIR/CNI+		N	-	-	-	-	-	-	-
		(3) CE/CNI-		N	-	-	-	-	-	-	-
		(4) CE/CNI+		Y	SRI4	13.58	CI	Mes	Y	1	Y
Sub-010	SRJ	(1) FLAIR/CNI-	M	Y	SRJ1	5.91	Ne	PN	N	-	N

continued on next page

Patient number	Tumornname	Tumor localization	Sex	Biopsies (Y/N)	Sample name	Biopsy GSC content (BGC) at day 0 (%)	Biopsy molecular classification		Stable primary-NS generation (Y/N)	Time to NS (TTN) generation (days)	Stable secondary-NS generation (Y/N)
							Verhaak (34) PN Ne Mes CI	Wang (35) PN Mes CI			
Sub-012	SRK	(2) FLAIR/CNI+	M	Y	SRJ2	10.02	PN	PN	N	–	N
		(3) CE/CNI–		Y	SRJ3	16.42	Mes	Mes	N	–	N
		(4) CE/CNI+		Y	SRJ4	54.13	Mes	Mes	Y	5	N
		(1) FLAIR/CNI–		Y	SRK3	6.02	Ne	PN	N	–	N
Sub-013	SRL	(2) FLAIR/CNI+	F	Y	SRK4	11.67	nd	nd	N	–	N
		(3) CE/CNI–		Y	SRK1	60.26	Mes	Mes	Y	8	Y
		(4) CE/CNI+		Y	SRK2	68.53	CI	CI	Y	8	Y
		(1) FLAIR/CNI–		Y	SRL4	23.27	Ne	PN	Y	21	Y
Sub-014	SRM	(2) FLAIR/CNI+	M	Y	SRL3	36.27	Ne	PN	Y	13	Y
		(3) CE/CNI–		Y	SRL1	63.64	Mes	CI	Y	13	Y
		(4) CE/CNI+		Y	SRL2	79.55	Ne	CI	Y	21	Y
		(1) FLAIR/CNI–		Y	SRM1	14.02	nd	nd	Y	18	Y
Sub-015	SRN	(2) FLAIR/CNI+	M	Y	SRM3	16.03	Ne	PN	Y	19	Y
		(3) CE/CNI–		N	–	–	–	–	–	–	–
		(4) CE/CNI+		Y	SRM2	42.07	CI	CI	Y	5	Y
		(1) FLAIR/CNI–		Y	SRN3	3.87	Ne	PN	N	–	N
Sub-017	SRO	(2) FLAIR/CNI+	M	Y	SRN4	15.94	PN	PN	Y	4	Y
		(3) CE/CNI–		Y	SRN1	3.97	PN	PN	Y	11	Y
		(4) CE/CNI+		Y	SRN2	13.04	PN	PN	Y	28	Y
		(1) FLAIR/CNI–		Y	SRO3	10.71	Ne	CI	Y	14	Y
Sub-019	SRQ	(2) FLAIR/CNI+	M	Y	SRO2	5.45	PN	PN	Y	10	Y
		(3) CE/CNI–		Y	SRO1	7.46	Mes	Mes	Y	5	Y
		(4) CE/CNI+		N	–	–	–	–	–	–	–
		(1) FLAIR/CNI–		Y	SRQ2	5.55	Ne	PN	Y	33	N
Sub-020	SRR	(2) FLAIR/CNI+	M	N	–	–	–	–	–	–	–
		(3) CE/CNI–		Y	SRQ3	42.05	PN	PN	Y	33	N
		(4) CE/CNI+		N	–	–	–	–	–	–	–
		(1) FLAIR/CNI–		Y	SRR2	4.04	CI	CI	Y	13	N
		(2) FLAIR/CNI+		Y	SRR4	19.11	CI	CI	Y	13	N
		(3) CE/CNI–		Y	SRR3	4.92	Ne	PN	Y	18	N
		(4) CE/CNI+		Y	SRR1	10.69	CI	CI	Y	15	N

continued on next page

Patient number	Tumorname	Tumor localization	Sex	Biopsies (Y/N)	Sample name	Biopsy GSC content (BGC) at day 0 (%)	Biopsy molecular classification		Stable primary-NS generation (Y/N)	Time to NS generation (TTN) (days)	Stable secondary-NS generation (Y/N)
							Verhaak (34) PN Ne Mes CI	Wang (35) PN Mes CI			
Sub-021	SRS	(1) FLAIR/CNI-	M	Y	SRS3	4.7	Ne	PN	Y	8	Y
		(2) FLAIR/CNI+		Y	SRS2	13.37	CI	CI	Y	8	Y
		(3) CE/CNI-		Y	SRS1	12.87	CI	CI	Y	8	Y
		(4) CE/CNI+		Y	SRS4	8.34	PN	PN	Y	8	Y

compared to CNI- biopsies. As a consequence, we also studied whether or not these biopsies gave rise to GSC-enriched NS more or less rapidly depending on their CNI origin. By determining the time-to-NS (TTN) formation (in days), we noticed, in our 11 analyzable pairs of FLAIR biopsies, a clear tendency for FLAIR/CNI+ samples to generate NS faster (median = 13 days) compared to their CNI- counterparts (18 days) (Fig. 3E and table S5). Beyond paired biopsies, when all the samples are considered, a significant ($P = 0.01759$) shortening of the TTN was observed in FLAIR/CNI+ compared to FLAIR/CNI- biopsies, very close to the TTN observed in CE/CNI- and CE/CNI+ groups (table S5 and fig. S3). Notably, between these two last groups, no significant differences could be shown (Fig. 3F, table S5, and fig. S3), as well as between CNI- and CNI+ groups (regardless of their CE/FLAIR origin) and between FLAIR and CE groups (regardless of their CNI status) (fig. S3). In line with a faster appearance of GSC-enriched NS in FLAIR/CNI+ samples, we found a clear trend for FLAIR/CNI+ biopsies to generate stable primary and secondary NS (84.6 and 69.2%, respectively) with a better yield than FLAIR/CNI- biopsies (69.2 and 42.9%). Notably, the NS generation rates of FLAIR/CNI+ samples are quite similar to those observed in CE biopsies, regardless of their CNI status (table S5). In secondary NS, the clonogenic potential was also measured as the percentages of GSCs able to generate NS (table S2). We observed a slight and not-significant increase in this clonogenic potential in CNI+ GSC, both from FLAIR and CE samples (table S5). To sum up, concerning the pattern of NS generation, it appears that FLAIR/CNI+ tumor zones, contrary to FLAIR/CNI-, may contain a sufficient subpopulation of GSC to rapidly produce GSC-enriched NS, similarly to CE biopsies, which contain a greater subpopulation of GSC.

Tumorigenicity potential of GSC coming from different areas

We have also studied the tumorigenic potential of the secondary NS generated from each tumor areas because GBM cell tumorigenicity in orthotopically xenografted nude mice was shown as a major property of GSC (11). For each primary GSC line able to generate stable secondary NS ($n = 34$ of 54), NS-dissociated cells were subjected to orthotopic xenografts in female nude mice ($n = 3$ to 7 mice per NS sample) to assess their tumorigenic potential. They all generated brain tumors to varying degrees, with a tumor penetrance

rate between 50 and 100% according to the NS cell line (table S3). We observed no significant differences for this parameter between FLAIR/CNI- and FLAIR/CNI+ and between CE/CNI- and CE/CNI+. The GSC-derived tumors were analyzed by hemalum staining and Nestin immunostaining to confirm their tumorigenic ability (fig. S4). By analyzing the global median OS in xenografted mice as a quantitative variable [in days (95% CI)], we observed that GSC obtained from FLAIR/CNI- NS were associated ($P = 0.03159$) with an increased median OS [206 (127 to 420)], compared to the mice implanted with FLAIR/CNI+ NS-derived cells [182 (145 to 232)] or with CE NS-derived cells [189 (142 to 227) for CE/CNI- and 188 (152 to 270) for CE/CNI+] (table S6A). Univariate analysis by log-rank test confirmed that OS in mice xenografted with FLAIR/CNI+ NS-derived cells is significantly ($P = 0.0448$) lower than in the FLAIR/CNI- group (Fig. 4A), with a survival rate at $t = 250$ days of 42.9% versus 17.5% for FLAIR/CNI- and FLAIR/CNI+ groups, respectively (table S6A). On the contrary, no significant differences could be highlighted between CE/CNI- and CE/CNI+ groups, between CNI- and CNI+ mice (irrespective of the FLAIR/CE origin), or between CE and FLAIR conditions (irrespective of the CNI pattern) (Fig. 4, B to D). The detailed OS for each xenografted mouse, allocated by patient and tumor subgroups, is shown in fig. S5. We also analyzed the impact of the sex of the patient cell line on mice OS and did not observe any significant effects in the whole population and in our different subgroups (FLAIR, CNI-, or CNI+) with the exception of the CE GSC subgroup, in which female cell lines present a lower OS compared to GSC established from male patients (table S6B). To summarize, FLAIR/CNI+-derived NS, which are generated in vitro from tumor biopsies faster than FLAIR/CNI- samples (13.36 ± 1.54 versus 27.67 ± 5.78 as day averages \pm SEM, respectively), also appear to give rise to tumors more rapidly in xenografted mice.

Radiosensitivity of GSC according to different zones of biopsy

As GSC phenotype is associated with increased radioresistance and because we have shown that CNI2 areas were predictive of the site of relapse after RT, we also checked whether GSC cell lines coming from CNI+ area had a decrease in radiosensitivity compared to those coming from CNI- area. For that, the in vitro radiosensitivity of each stable NS cell line was studied by realizing clonogenic assays

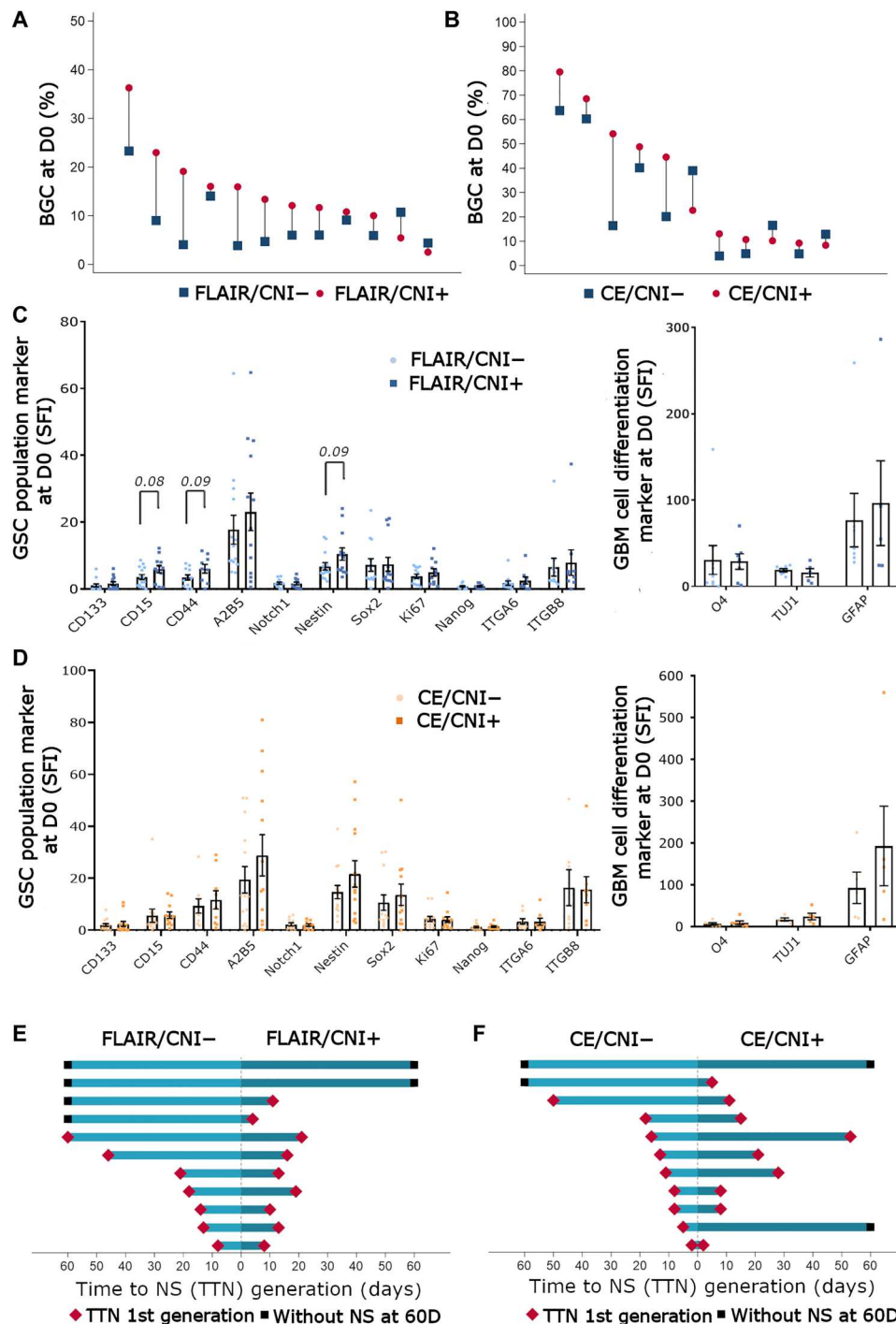


Fig. 3. FLAIR/CNI+ biopsies are characterized by an enrichment in the GSC subpopulation and a shorter time to NS generation compared to FLAIR/CNI- biopsies. (A and B) Pairwise comparison of the biopsy GSC content at day 0 (D0) after surgery (BGC%), as determined by FACS, either in FLAIR/CNI- and FLAIR/CNI+ (A) or in CE/CNI- and CE/CNI+ (B) samples. Detailed pair by pair comparisons between the two biopsy groups were shown. (C and D) Immunofluorescence analysis performed by FACS for the indicated stem (left) and differentiation (right) markers in the GSC subpopulation analyzed at D0 either in FLAIR/CNI- and FLAIR/CNI+ (C) or in CE/CNI- and CE/CNI+ (D) samples. The SFI (specific fluorescence index), used to evaluate the marker expression level, were expressed as means \pm SEM of all analyzed samples. (E and F) Pairwise comparison of the TTN generation, either in FLAIR/CNI- and FLAIR/CNI+ (E) or in CE/CNI- and CE/CNI+ (F) samples.

at increasing IR doses and subsequently establishing their MID (mean inactivation dose). We did not observe any significant differences between FLAIR/CNI– and FLAIR/CNI+ NS or between CE/CNI– and CE/CNI+ NS (table S7).

Relationship between GSC-associated pattern in CNI–/+ biopsies and patient outcome

FLAIR/CNI+ tumor areas, which were found by our team to predict the site of GBM relapse after chemo-RT, appeared to be enriched in GSC and to give rise more rapidly to stable NS in restrictive culture conditions, compared to FLAIR/CNI– biopsies. To find out a possible link between the previously described GSC-related parameters in the biopsies and patient outcome, we studied OS and PFS for our 16 patients according to their biopsy GSC content (BGC%, determined by FACS at day 0) or to their TTN generation. Concerning BGC and TTN, patients were dichotomized into two distinct groups according to the median values observed in FLAIR/CNI+ biopsies. Univariate analysis of OS and PFS by log-rank test highlighted a significant association of high BGC with decreased OS ($P = 0.0112$) and PFS ($P = 0.0057$) (Fig. 5, A and B, and table S8, A and B). This was confirmed by analysis through a Cox statistical model using continuous variables (table S8, A and B). Notably, if we use for each patient the maximum BGC of both FLAIR biopsies (CNI– and CNI+), then the same type of association between low OS/PFS and high BGC is found with the Cox model and the log-rank test, with a loss of statistical significance in the latter case (table S8, A and B). Focusing on the TTN parameter, univariate analyses using the Cox model did not show a significant association between OS/PFS and TTN in days, although there is a trend in this direction for FLAIR/CNI+ samples (table S9, A and B). We then refined this TTN parameter to analyze both OS and PFS according to their ability to generate or not stable primary NS at 14 days after surgery and culture in stem medium (PN14), because only 27.3% of FLAIR/CNI– biopsies could generate NS at 14 days compared to 50% in FLAIR/CNI+ (table S5). Log-rank test analysis of OS/PFS according to PN14 parameter in FLAIR/CNI+ depicted a significant association of PN14+ capacity with a decreased OS ($P = 0.0190$) and a strong tendency with a reduced PFS ($P = 0.0606$) (Fig. 5, C and D, and table S10, A and B). Notably, if FLAIR/CNI+ GSC-related parameters (BGC and PN14) were correlated with reduced OS and PFS, it was not the case for CE biopsies, regardless of their CNI status (tables S8 and S10). Consequently, FLAIR/CNI+ tumor areas specifically appear to be predictive of GBM patient outcome when considering their relative GSC-enrichment.

RNA-seq analysis of patient's biopsies

In light of the previous results, it appears that FLAIR/CNI+ tumor areas, predictive of the site of relapse in patients with GBM, have specific biological (higher GSC content, faster primary-NS generation), preclinical (increased tumorigenicity in mice), and clinical properties (correlation of patient PFS/OS with biological parameters). To observe these clinico-biological results through the prism of molecular characterization, we performed an RNA-seq analysis of all available biopsies (51 of 54 samples), including 13 of 14 FLAIR/CNI–, 12 of 13 FLAIR/CNI+, 14 of 14 CE/CNI–, and 12 of 13 CE/CNI+ samples. Expression dataset were first used to determine the molecular subtype of each biopsy (Table 2) according to either Verhaak or Wang classification (34, 35). Using Verhaak classification, samples could be classified into four molecular

subgroups (Ne, Neural; PN, proneural; Mes, Mesenchymal; Cl, Classical), and the results show that CE biopsies are mainly from Mes and Cl subclasses (62.96%) and quite homogeneous between CNI– and CNI+ areas (fig. S6). However, in FLAIR peritumor zone, we observe a majority of PN and Ne subclasses (70.37%) and a marked difference between FLAIR/CNI– and FLAIR/CNI+ zones. FLAIR/CNI– biopsies were predominantly classified as Ne subtype (78.57%), while FLAIR/CNI+ tumor samples were divided into three equivalent groups (30.77% of PN, Ne, and Cl subtypes). As demonstrated by Wang *et al.* in 2017 (35), it appeared that the Neural subgroup is in fact nontumor specific and is due to normal neural lineage contamination, frequently encountered at the tumor margin. In light of this observation, it is worthwhile to consider that Ne subclass is overrepresented in FLAIR/CNI– biopsies compared to FLAIR/CNI+ samples, which could mean that FLAIR/CNI+ peritumor areas are enriched in cancer cells contrary to FLAIR/CNI– zones. To assess this hypothesis, we analyzed pre-operative diffusion MRI metrics in each patient to determine the apparent diffusion coefficient (ADC) on each FLAIR biopsy location. Reduced ADC is observed in patients with GBM because of an increased tumor cellularity (36). In FLAIR tumor regions, we coregistered CNI and ADC metrics (table S11A) and observed a significantly reduced ADC in FLAIR/CNI+ biopsy locations compared to FLAIR/CNI–. Moreover, we noted a negative correlation between CNI and ADC in FLAIR biopsy locations (fig. S7 and table S11B). Concerning molecular classification, we also used the Wang classification, using the Gliovis data portal (37), to refine the molecular classification into three different and more tumor-specific subgroups: PN, Mes, and Cl. We observed that the same patient, according to the biopsy location, could present up to three different subtypes (Table 2). As shown in Fig. 6A, FLAIR biopsies were mainly classified as PN (59.26%) and Cl (29.63%), and CE samples as Mes (40.74%), Cl (29.63%), and PN (25.93%). It should be noted that no significant differences in the molecular Wang subclasses could be observed when comparing CNI– and CNI+ biopsies, either in FLAIR, CE, or FLAIR+CE areas (Fig. 6A).

Beyond this molecular classification, from principal components analysis (PCA) of the expression data generated from the four tumor groups, we found a clear separation of tumor samples from CE and FLAIR samples along the first principal component PC1 (accounting for 20.06% of the total variance), while CE/CNI– and CE/CNI+ clusters were globally overlapping along PC1 and PC2 (2d principal component, accounting for 10.61% of the total variance) (Fig. 6B). Moreover, we noticed that 7 of 13 FLAIR/CNI– samples segregated from the three other groups along PC1. When only FLAIR/CNI– and FLAIR/CNI+ biopsies were taken into account through PCA, we observed more clearly this separation along PC1, with three different clusters: seven FLAIR/CNI– biopsies on a side, three FLAIR/CNI+ samples on the other side, and a common cluster between the two (Fig. 6B). Then, PCA suggests that RNA-seq analysis may reveal two levels of differential expression: FLAIR versus CE, irrespective of CNI pattern, and FLAIR/CNI– versus FLAIR/CNI+. A differential expression analysis was subsequently carried out through DESeq2 and MA plots were generated, on the basis of the thresholds of an adjusted q value < 0.05 and a \log_2 fold change ≥ 2 . These MA plots revealed that no differential gene expression could be shown either between CE/CNI– and CE/CNI+ subgroups or between CNI– and CNI+ groups, irrespective of the FLAIR/CE origin. However, 4003 differential

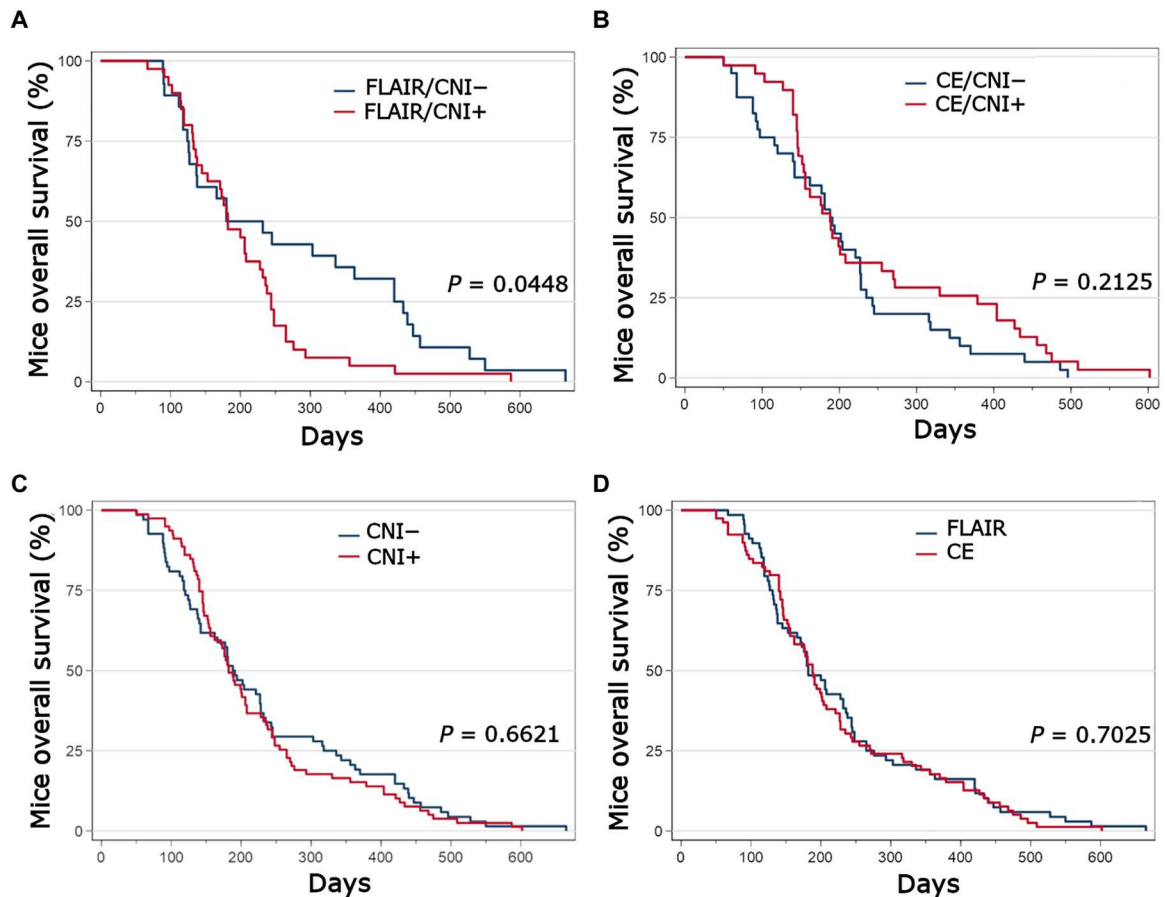


Fig. 4. GSC primary cell lines obtained from FLAIR/CNI+ biopsies are associated with increased tumorigenesis in xenografted mice compared to FLAIR/CNI– NS. (A to D) For each primary GSC cell line able to generate stable secondary NS, NS-dissociated cells were subjected to orthotopic xenografts in nude mice ($n = 3$ to 7 mice per sample). OS data were determined for each GSC group (FLAIR/CNI–, FLAIR/CNI+, CE/CNI–, and CE/CNI+) to assess their tumorigenic ability. (A to D) Kaplan-Meier curves for OS in mice xenografted with the indicated GSC subgroups. Exact P values for FLAIR/CNI– versus FLAIR/CNI+ (A), CE/CNI– versus CE/CNI+ (B), CNI– versus CNI+ (C), or FLAIR versus CNI (D) group comparisons were determined by log-rank analysis.

expressed genes were statistically highlighted between FLAIR and CE groups and 565 between FLAIR/CNI– and FLAIR/CNI+ subgroups (Fig. 6C).

To further explore the differential pattern in FLAIR area between CNI– and CNI+ biopsies, Kyoto Encyclopedia of Genes and Genomes (KEGG) and Hallmark pathway enrichment analyses were also performed, which revealed that differentially expressed genes were mainly involved in DNA repair, cell cycle and DNA/RNA-related processes, adhesion/migration and extracellular matrix (ECM)–related pathways, and angiogenesis and stemness/EMT (epithelial-to-mesenchymal transition), with a clear enrichment of all these pathways in FLAIR/CNI+ biopsies (Fig. 6D). When focusing on some specific KEGG pathways—Cell Cycle/P53 signaling pathways and ECM Receptor-interaction/Focal Adhesion (FA)—we could observe a strong overexpression of major regulator genes in FLAIR/CNI+ biopsies. For example, considering Cell cycle/P53 pathways, *CDK1/2/4*, *PLK1*, *ATR*, *CHEK1*, *TP53*, and *WEE1* were shown to be significantly overexpressed in FLAIR/CNI+ samples. All of these genes were demonstrated to have major roles in GBM progression (Fig. 6E). By looking at FA/ECM receptor interaction pathways, many genes coding for matrix

components (collagen, laminin, fibronectin, tenascin, etc.), integrins (*ITGA1/A3/A4/A7*), and Rho–guanosine triphosphatases (GTPases) activating pathways (*VAV1/3*) were overexpressed in FLAIR/CNI+ areas compared to FLAIR/CNI– (Fig. 6E). To refine this enrichment analysis and to observe in detail which biological processes were differentially represented between these two groups, we also conducted Reactome and Gene Ontology Biological Processes (GO BP) pathway enrichment analyses (Fig. 7, A and B). Supervised (FLAIR/CNI– versus FLAIR/CNI+) and unsupervised analyses revealed a clear and significant enrichment of stemness/EMT-related pathways (NOTCH and Hippo pathways notably) and adhesion/migration/ECM interaction (relative among others to integrins, Rho-GTPases, collagen, and laminin). Moreover, concerning metabolic pathways, we noticed an enrichment of Cho-related pathways and a depletion of aspartate metabolic pathways in FLAIR/CNI+, in accordance with the MRSI parameters established to specifically collect low- and high-CNI areas within tumor and peritumor area (Fig. 7, A and B). Considering other metabolic pathways, we have also observed an important enrichment of mitochondria-related bioenergetic pathways in

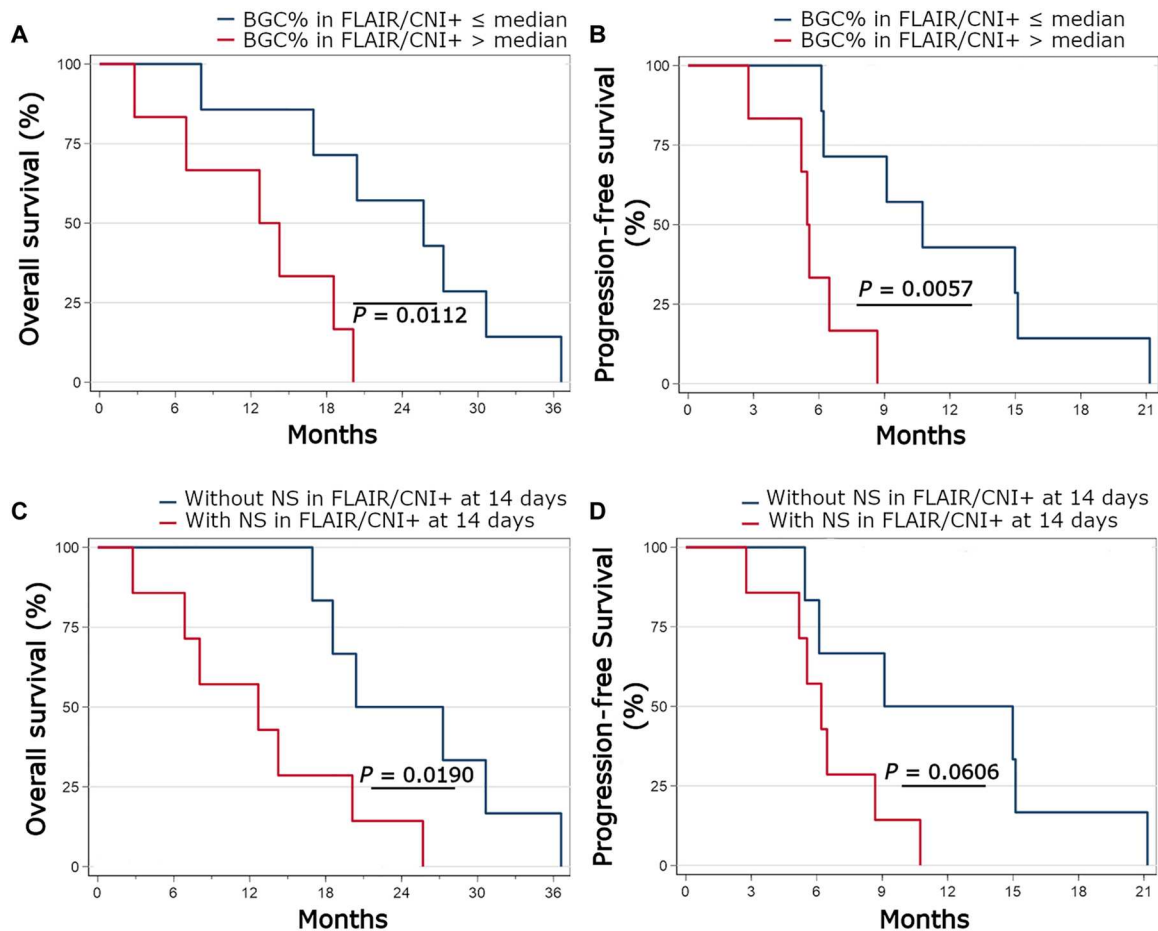


Fig. 5. Higher BGC and increased ability to promptly generate primary NS in FLAIR/CNI+ samples are two biological parameters associated with worse patient outcome. (A and B) Kaplan-Meier curves for OS (A) and PFS (B) in patients with GBM enrolled in the SEMRI trial when dichotomized into two distinct groups according to the median BGC values observed in FLAIR/CNI+ biopsies. (C and D) Kaplan-Meier curves for OS (C) and PFS (D) in patients with GBM when dichotomized into two distinct groups according to FLAIR/CNI+ biopsies' ability to generate or not stable primary NS in stem medium at 14 days after surgery. (A to D) Exact *P* values were determined by log-rank analysis.

FLAIR/CNI+ biopsies associated to a lower representation of glycolytic pathways (Fig. 7A).

As our biological and preclinical results demonstrated a significant increase of GSC subpopulation and GSC-related properties in FLAIR/CNI+ tumor areas compared to FLAIR/CNI−, which was confirmed at the molecular level through Hallmark (Fig. 6, D to F), GO BP, and Reactome (Fig. 7, A and B) pathway enrichment analyses, we also set up some specific gene signatures to study the enrichment of each areas for either GSC subpopulation or neural-differentiated lineages (oligodendrocytes, neurons, and astrocytes), based on our previous papers on the GSC compartment (33, 38) and the related literature (3) (Fig. 8A and table S12). We observed a significant enrichment of the stem-specific signature in FLAIR/CNI+ biopsies and, on the contrary, an enrichment trend for oligodendrocytic ($P = 0.065$) and neuronal ($P = 0.073$) signatures in FLAIR/CNI− zones, showing a strong increase of the undifferentiated/differentiated balance in FLAIR/CNI+ areas compared to FLAIR/CNI− (Fig. 8A). Notably, no significant differences could be seen for CE/CNI− versus CE/CNI+ or CNI− versus CNI+ subgroups. However, we found a significant decrease of all three differentiation

signatures in FLAIR samples compared to CE biopsies. At the gene level, on the basis of the RNA-seq results, we indeed observe an important up-regulation of numerous specific GSC-related genes (*SOX2*, *NES*, *NOTCH1*, *NG2*, *ITGA7*, *EZH2*, *BIRC5*, etc.) and a global decrease of oligodendrocytic genes (*CNP*, *OMG*, *MAL*, *MBP*, *OLIG1*, etc.) in FLAIR/CNI+ samples (Fig. 8B and fig. S8A). Several astrocytic (*S100B*, *NDRG2*, etc.) and neuronal (*NEFM* and *SNCA*) genes were also decreased in FLAIR/CNI+ biopsies, but no clear trend could be highlighted (fig. S8, B and C). Notably, when we consider GSC, oligodendrocytic and astrocytic markers, it appears that the global expression levels in FLAIR/CNI+ biopsies are quite close to those found in CE/CNI− or CE/CNI+ samples, with no significant differences between the latter two groups (Fig. 8B and fig. S8).

DISCUSSION

Because of major intratumoral heterogeneity and high cellular plasticity, GBM is one of the most difficult solid tumors to manage and treat. As recurrence is almost systematic, determining the tumor

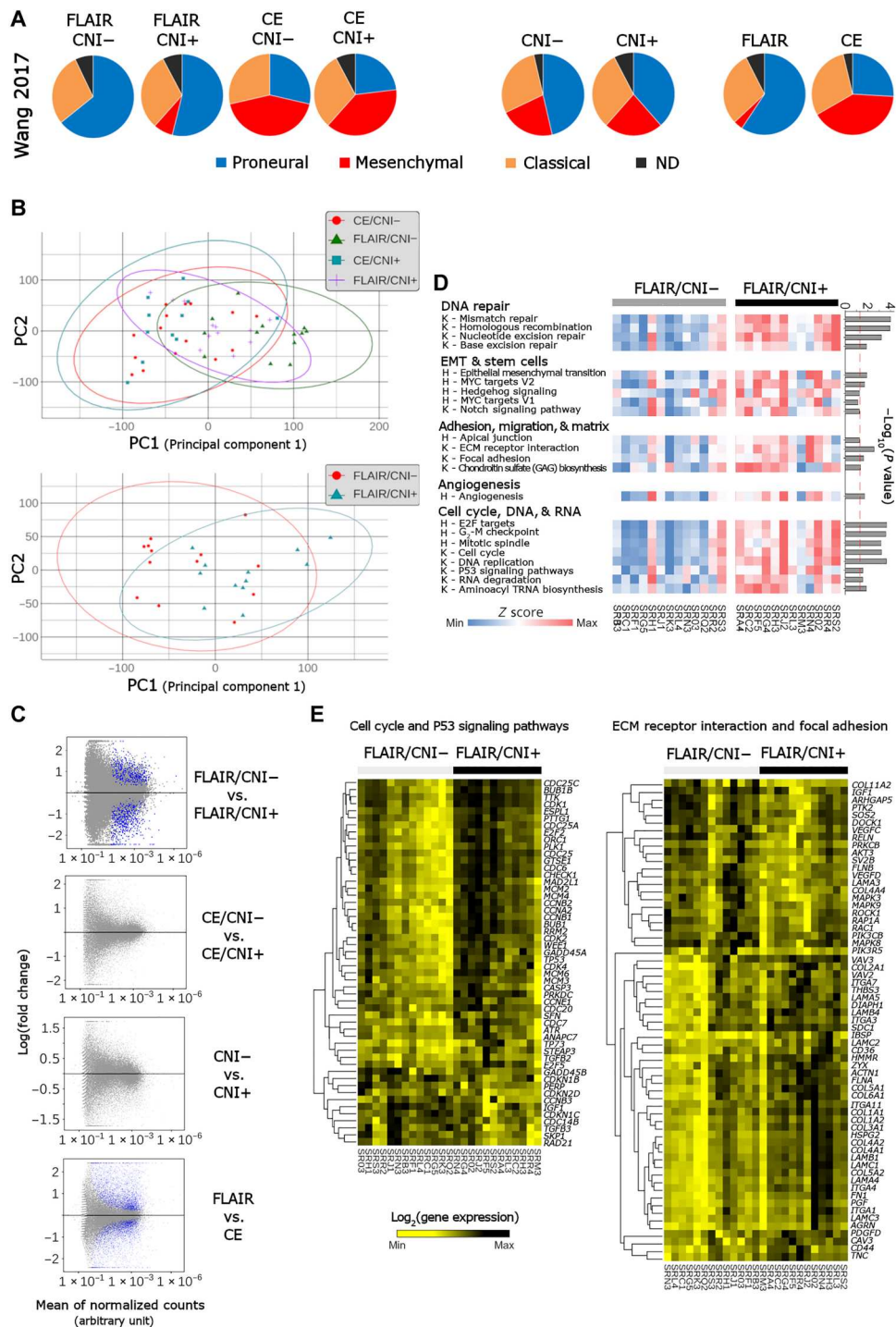


Fig. 6. RNA-seq analyses revealed that FLAIR/CNI+ biopsies were enriched in gene signatures related to stemness/epithelial-to-mesenchymal transition, migration/adhesion, and cell cycle/DNA repair pathways compared to FLAIR/CNI+ tumor samples. RNA-seq analyses were conducted on the 51 available tumor biopsies obtained from 16 patients with GBM and segregated into four different groups (FLAIR/CNI-, FLAIR/CNI+, CE/CNI-, and CE/CNI+). (A) Molecular classification of GBM biopsies of each indicated group according to Wang classification. ND, not determined. (B) PCA of RNA-seq profiles of the four different biopsy groups (top) or restricted to FLAIR/CNI- and FLAIR/CNI+ samples only (bottom). (C) MA plots were generated after a differential expression analysis between the indicated biopsies groups, based on the thresholds of an adjusted q value <0.05 and a \log_2 fold-change ≥ 2 . Blue dots indicate differentially expressed genes. (D and E) KEGG (K) and Hallmark (H) pathway enrichment analyses were performed on FLAIR/CNI- versus FLAIR/CNI+ biopsies and showed the statistically significant up-regulation of indicated pathways (D). Differentially expressed genes in specified KEGG pathways were also represented in a supervised analysis between these two groups (E).

prognosis, the response to radio/chemotherapy, the site of recurrence, and the degree of tumor invasion are crucial challenges. For more than two decades, MRSI combined to conventional MRI has allowed a better understanding of GBM heterogeneity through the determination of some key metabolites at tumor and peritumoral levels (13, 39). Specific metabolites [such as Chol, NAA, lactate (Lac), lipids, myoinositol (mIns)] or metabolite ratios [such as Cho/NAA, Cho/Cr (creatinine) or Lac/NAA] have been shown to improve assessment of GBM diagnosis, progression, prognosis, and response to treatment, notably to RT. A recent study showed that MRSI can also appreciate, in a preclinical mouse model, the cell death response after IR, through malate/fumarate detection (40). More specifically, increased CNI and/or Cho/Cr ratio showed great benefit in discriminating glioma grades (41), tumor progression versus RT-induced changes (pseudoprogression or radionecrosis) (13, 42–45) and in highlighting GBM invasion front (25). In addition, CNI was proved to be useful after postoperative RT to assess the prognosis of GBM at recurrence, because CNI increase before, during, and/or after RT was associated with early GBM progression and bad prognosis (46, 47), notably within the peritumoral/FLAIR edema (20). In line with this, we previously showed that metabolically active CNI > 2 regions in both CE and FLAIR areas of pre-RT scans were predictive of the site of relapse after RT (14).

Considering these clinic specificities of CNI+ areas, we designed the STEMRI trial to understand what kind of cellular heterogeneity could sustain such metabolic particularities within the tumor and lead to these localized recurrence zones. We notably focused on the role of GSC because this stem-like cell population was demonstrated to largely mediate recurrence after radiochemotherapy. Here, we demonstrate that FLAIR/CNI+ biopsies contained twice larger amount of GBM cells in a stem-cell state compared to FLAIR/CNI– samples (median BGC: 6% versus 12%) and give rise, in restrictive stem medium, to specific GSC-enriched NS structures faster than FLAIR/CNI– biopsies (median TTN: 13 days versus 21 days) (Fig. 3, figs. S2 and S3, and tables S4 and S5). These FLAIR/CNI+ GSC analyzed by FACS just after surgery seem to overexpress stem markers only quite marginally compared to their CNI– counterparts. These features are only observed in FLAIR area, because CE biopsies, either CNI– or CNI+, have not significantly different BGC (16.5 and 22.7%, respectively) and TTN (9.5 and 8 days, respectively). Notably, despite a higher content of GSC and a slight overexpression of several stem markers [such as CD44 (32), Nestin (7), or Sox2 (5)] in CE biopsies compared to FLAIR samples (median BGC = 12.1% in FLAIR/CNI+), the TTN in both CE/CNI– and CE/CNI+ is relatively similar to TTN in FLAIR/CNI+ samples (13 days). It could be hypothesized that when a threshold BGC value is raised in the biopsy, the delay to generate NS in vitro may be approximately the same.

At the molecular level, RNA-seq analysis confirmed these biological observations, with a differential expression analysis revealing major differences in gene expression only between FLAIR/CNI– and FLAIR/CNI+ samples and between CE and FLAIR biopsies. Focusing on FLAIR samples, we demonstrated that CNI+ samples present an enrichment in stemness/EMT-associated pathways, either through the use of GO BP/Reactome/Hallmark-related signatures (Figs. 6D and 7, A and B) or through the determination of SES (sample enrichment score) for a self-designed dedicated GSC signature (Fig. 8A). Among these signatures, pathways related to

NOTCH, MYC, HEDGEHOG, and Hippo/YAP/TAZ appeared to be enriched in FLAIR/CNI+ samples. All these pathways were shown to be major actors to sustain stemness in GSC (48–52). In addition, in FLAIR/CNI+ biopsies, many stem-related genes were significantly overexpressed (Fig. 8B) and among them SOX2, which was previously shown to be increased at the protein level in high-CNI tumor areas in GBM (28). On the contrary, we showed that oligodendrocytic and neuronal differentiation signatures and related genes were enriched in FLAIR/CNI– biopsies.

Besides this stem/differentiation balance, our GO BP analyzes also reveal a significant enrichment in FLAIR/CNI+ zones for oxidative mitochondrial metabolic pathways in detriment of glycolytic processes. In this respect, the energetic metabolism in GSC appears to be very plastic and to rely partly on oxidative phosphorylation and not predominantly on glycolysis like differentiated GBM cells (53–55). Moreover, we showed that FLAIR/CNI+ bulk samples overexpressed numerous gene signatures (KEGG, GO BP, and Reactome) related to cell adhesion, migration, and interaction with ECM. It has been described that GSC have an increased ability to adhere, migrate, and invade compared to their differentiated counterparts (56, 57) but also that those capacities may vary according to the anatomical location of the biopsy, because GSC generated from the GBM peritumoral area displayed a higher migratory and invasive phenotype compared to GSC isolated from the tumor mass (58). In a recent study associating MRSI and RNA-seq of tumor bulks both in patients with GBM and in paired patient-derived orthotopic xenografts (PDOXs) (59), it was pointed out (i) that there was a good concordance between metabolite profiles recorded by MRSI in patients and the metabolite profiles observed during PDOX growth and (ii) that this tumor growth and related metabolic profiles (notably high Cho-containing compounds and low NAA), both in human and PDOX, were associated at the molecular level with an enrichment in signatures dedicated to adhesion, invasion and ECM, consistent with our results. All these observations lead us to hypothesize that GSC-enriched NS isolated from FLAIR/CNI+ areas might exhibit higher migratory/invasive and metabolic heterogeneity that could be monitored by at least RNA-seq and MRSI on cells (60) and in xenografted models (29, 59). These results could then be translated and validated at the clinical level through their specific therapeutic targeting to in fine improve radiochemotherapeutic response.

In complement to the overexpression of these different pathways in FLAIR/CNI+ bulk samples, we have shown that the NS coming from FLAIR/CNI+ biopsies were generated in vitro faster than their CNI– counterparts (shorter TTN) but also that these NS were more tumorigenic in orthotopically xenografted mice (Fig. 4A). Although no significant difference can be highlighted between stem markers at day 0 in FLAIR/CNI– versus FLAIR/CNI+ GSC, this could suggest, because tumorigenicity is a main characteristic of stem-cell state (4, 11), that primary-NS cell lines generated from FLAIR/CNI+ areas may have more robust stem cell-like traits than FLAIR/CNI– NS. Notably, one of the characteristics of GSC compared to more differentiated GBM cells is their strong radioreistance. However, we failed to observe a higher MID in FLAIR/CNI+ NS, despite an enrichment in GO BP signatures associated with response to RT in FLAIR/CNI+ bulk biopsies (Fig. 7A). One of the main challenges for future studies will be to explore more specifically stem-related properties of both FLAIR/CNI– and FLAIR/CNI+ GSC, particularly through RNA-seq analyses and

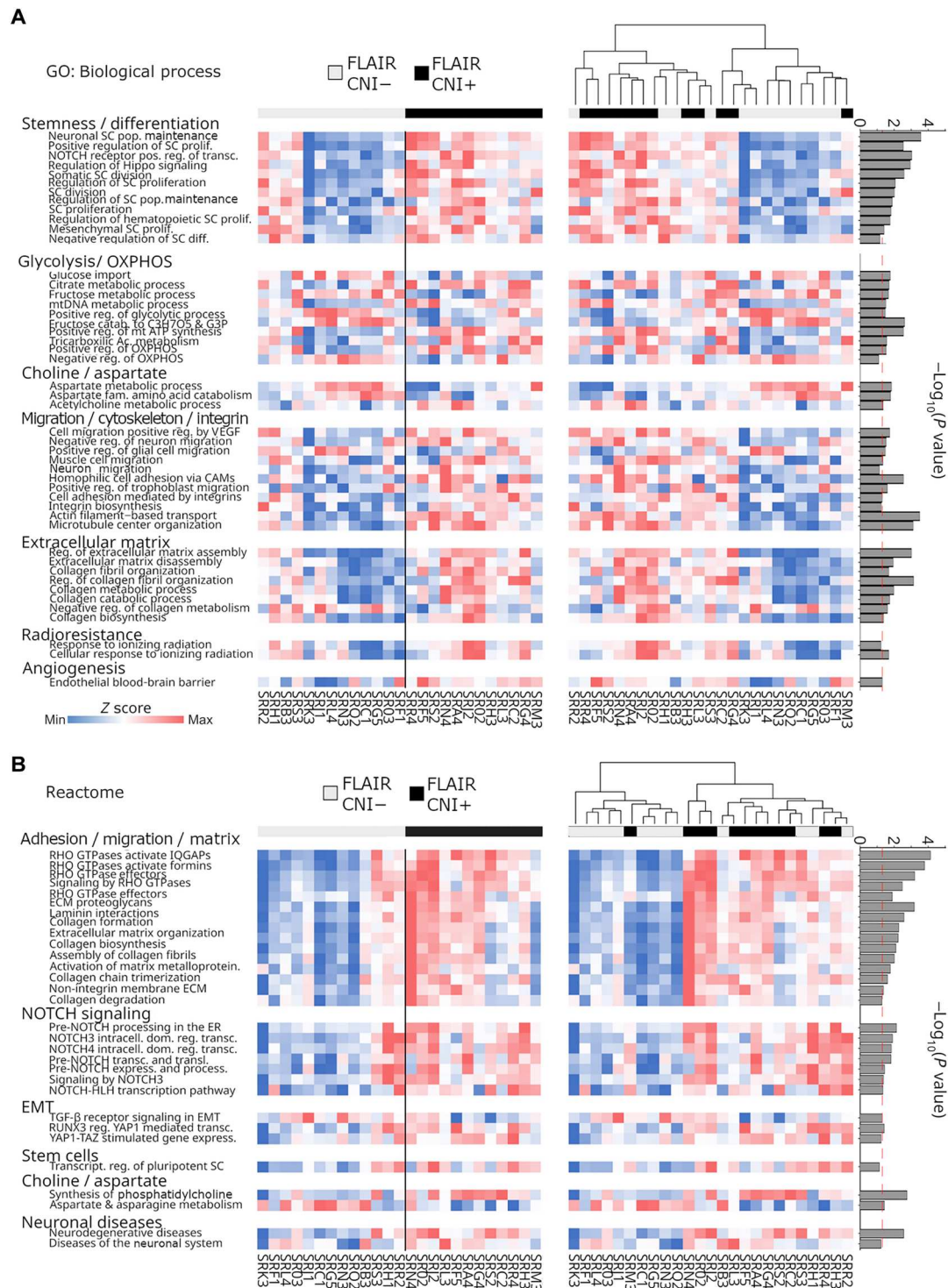


Fig. 7. Reactome and GO pathway enrichment analysis of RNA-seq data of FLAIR biopsies revealed that FLAIR/CNI+ biopsies were enriched in gene signatures related to stemness/EMT, migration/adhesion, and mitochondria-related bioenergetic pathways compared to FLAIR/CNI+ tumor samples. RNA-seq analyses were conducted on the 25 available tumor biopsies obtained from 16 patients with GBM and segregated into two different groups (FLAIR/CNI- and FLAIR/CNI+). (A and B) GO BP (A) and Reactome (B) pathway enrichment analyses were performed on FLAIR/CNI- versus FLAIR/CNI+ biopsies and showed the statistically significant differential expression pattern of specified gene signatures through both supervised (left) and unsupervised (right) analyses.

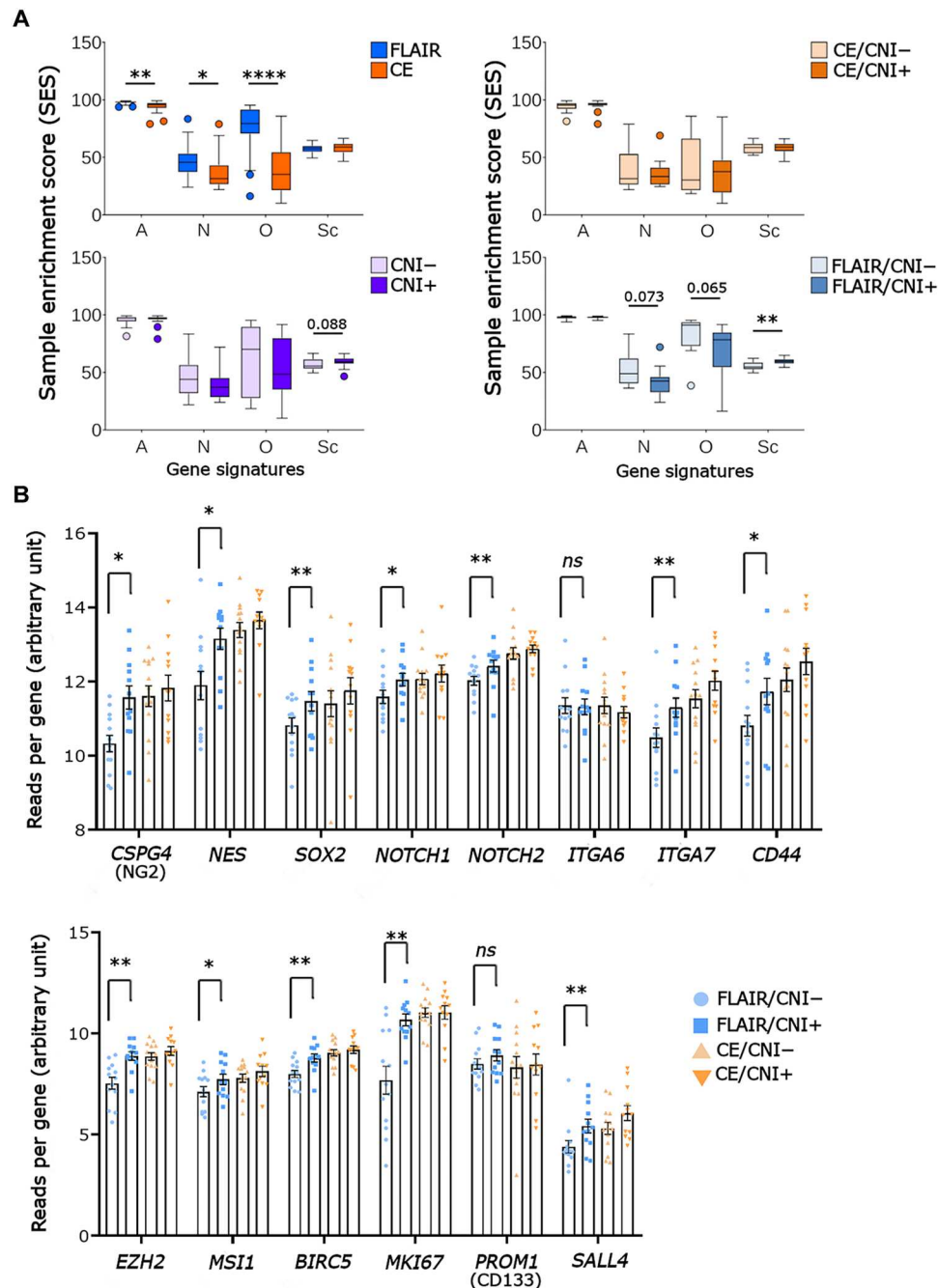


Fig. 8. RNA-seq-based analyses revealed a differential balance between stemness and differentiation-associated gene signatures between FLAIR versus CE samples and between FLAIR/CNI+ versus FLAIR/CNI- biopsies. RNA-seq analyses were conducted on the 51 available tumor biopsies obtained from 16 patients with GBM and segregated into four different groups (FLAIR/CNI-, FLAIR/CNI+, CE/CNI-, and CE/CNI+). (A) SES was calculated for specifically designed gene signatures: Astrocytes (A), Neurons (N), Oligodendrocytes (O), and Stem Cells (Sc) for the indicated biopsy groups. Boxplot diagrams of the median SES were shown. (B) Expression levels for specific GSC-associated genes in the four indicated biopsy subgroups were shown as means \pm SEM. * $P \leq 0.05$, ** $P \leq 0.01$, ns, not significant.

clonogenic limiting dilution assays, and to decipher whether or not CNI+ NS could better resist to chemotherapy or RT.

All these biological arguments are in favor of an increased stem population in FLAIR/CNI+ areas, along with a possible stronger stem state of these GSC. This specific pattern could also be due, at least partially, to a lower fraction of tumor cells in FLAIR/

CNI- tumor areas, as evoked by neural subgroup overrepresentation and lower ADC (figs. S6 and S7 and table S11), which could contribute to lower BGC%, weaker stem RNA-seq signature, and increased TTN in FLAIR/CNI- samples. Such an increase in GBM cells in stem state in FLAIR/CNI+ regions, combined with the fact that these tumor zones are associated in clinic with early progression, bad prognosis, and recurrence site prediction, strongly

suggests that it might be a correlation between our two biomarkers (BGC and TTN) and the clinical outcome of patients with GBM. Notably, previous works showed a significant negative correlation between NS generation ability and patient outcome (61–63), as well as between the expression of several stem markers, such as Nestin, CD133, EZH2, or Notch1, and patient outcome (64–69). In our study, we observed that BGC% at day 0 in FLAIR/CNI+ biopsy is inversely correlated with OS and PFS. In the same way, the TTN-derived parameter measuring the ability of FLAIR/CNI+ biopsy to generate primary NS at d14 (PN14) is also correlated with OS and PFS. We can therefore conclude that in FLAIR/CNI+ tumor areas, the determination of these two GSC-related parameters can predict patient outcome. Future clinical studies need to be performed to correlate these particular parameters to the pattern of relapse as defined by MRI/MRSI follow-up.

The correlation between stem-related parameters in clinic for GBM treatment to delay recurrence after surgery and radiochemotherapy. The gold-standard surgery for GBM is presently the “maximal safe resection” based on the maximal removal of CE tumor zones, without FLAIR-positive peritumoral area resection. It was previously shown that larger extent of CE gross total resection (notably in the range of 80 to 100%) is associated with improved patient outcome (70). However, recently supramaximal resection of both CE and FLAIR tumor zones was also experimented in large cohorts of patient with GBM. These trials demonstrated that minimal residual extent of non-CE tumor after surgery or higher removal extent of FLAIR-positive edematous infiltrative tumor area could translate into patient outcome benefits (70–72). However, the most important limitation of this type of surgical procedure is the possible manifestation of additional postoperative neurological deficits linked to the supramaximal resection of FLAIR tumor zones, which could significantly hamper the survival benefit seen in these patients (73). In the light of these recent clinical data and our present results, we can hypothesize that restricting the resection of the edematous and infiltrated non-CE zone to the FLAIR areas associated with GSC enrichment (i.e., here the CNI+ zones determined by MRSI) could certainly reduce the risk of postoperative neurological deficits and thus significantly increase patient outcome. Another strategy would be to boost the IR dose specifically on FLAIR/CNI+ zones. We recently conducted a phase 3 multicentric trial (SPECTRO GLIO) evaluating safety and efficacy of an IR boost (72 Gy versus 60 Gy) on these abnormal MRSI regions in newly diagnosed GBM but failed to show an improvement in patient survival outcome (74), with a median OS of 22.2 months, quite similar to the median OS (23 months) reported in a one-arm pilot study using a boost of 75 Gy on CNI+ zones (75). Notably, this pilot study showed a better PFS (16.6 months) than historical controls. This absence of effect, at least for OS, could be explained by a similar radioresistance of GSC cell lines in CNI– and CNI+ tumor areas (table S7), as well as a higher GSC content (BGC %) in these FLAIR/CNI+ zones (Fig. 3A). This IR boost, well tolerated, is probably not sufficient enough to hamper this GSC population and may be combined to other approaches (i.e., guided surgery and targeted therapy directed against biological pathways overexpressed in FLAIR/CNI+ areas that we brought to light in the present study). Beyond MRSI, we have recently demonstrated through preoperative perfusion and diffusion MRI that increased cerebral blood volume and low ADC could correlate respectively with high BGC% and shorter TTN in FLAIR biopsies (76). Then,

combining MRSI/MRI data with multimodal MRI (notably perfusion and diffusion MRI) could also help to target more precisely those particular FLAIR areas associated with higher recurrence and tumorigenesis and reduce neurological side effects. Last, by highlighting in CNI+ areas several major pathways that we have previously shown to be involved in resistance to RT, as EMT-related pathways, DNA repair–linked pathways, or pathways associated to adhesion/migration/ECM interaction (49, 77), these results also suggest that, beside using MRSI for guided surgery and RT target determination, association of inhibitors of these particular pathways in association with radiochemotherapy could also increase the efficacy of these treatments in the management of patients with GBM.

MATERIALS AND METHODS

Patients

Study approval

This trial was reviewed and approved by the institutional review board, the French ethics committee on 30 May 2012 (registration number 2012-A00585-38), and the French Drug Administration (ANSM) on 15 June 2012 (registration number B120639-40). All participants signed a written informed consent form (Fig. 1).

Study design

Between May 2013 and June 2017, 21 patients with newly diagnosed GBM have been enrolled in a prospective biomedical study of interventional type. This pilot study (ClinicalTrials.gov NCT01872221), combining a metabolic imaging approach (proton magnetic resonance spectroscopy or ¹H-MRSI) and a biological one, have been performed in patients with GBM to determine whether a particular MRSI marker of aggressiveness (CNI > 2, hereafter referred to as CNI+) can be associated with specific biological patterns as regards to GSC content.

In the first part of the study, patients with radiological criteria of GBM amenable to surgical resection have been selected by a preoperative committee and then included (Fig. 1). Preoperative multimodal MRI/MRSI scans have been done (CHU Purpan, Toulouse, France), and all data acquired have been integrated in the image-guided surgical device (i.e., neuronavigation system) to be used intraoperatively (cf. patient’s imaging paragraph for details). During tumor resection (CHU Purpan), tissue samples have been individualized on the basis of their multimodal imaging characteristics and processed for biological analysis (as described below). Notably, postoperative MRI was realized in the 72 hours following surgery and also before RT for treatment planning (at day 30 after surgery). In the second part, patients were treated after surgery by the standard radiochemotherapy Stupp (78) protocol (Institut Claudius Regaud, Toulouse, France) and then followed starting 1 month after the end of the chemo-RT phase, by clinical evaluation and multimodal MRI including MRSI every 2 months during the first year (CHU Purpan) and then every 3 months until progression (Fig. 1).

Study objectives

The study primary objective outcome was the capacity of GBM resected samples to form GSC-enriched NS *in vitro* as well as to form invasive brain tumor after orthotopic xenograft of the derived GSC population in nude mice. The *in vitro* capacity was assessed at the CRCT center (Toulouse, France) through several parameters: (i) the time necessary to generate NS after biopsy processing and culturing

and (ii) the GSC enrichment of the resected biopsies just after surgery, determined by GSC-subpopulation quantification through FACS analysis and by the determination of particular molecular stem signatures in resected samples through RNA-seq analysis. The in vivo capacity was both assessed by the percentage of GSC-implanted mice able to develop a brain tumor and the time to onset of tumor-associated neurological signs. The secondary objective outcome was the time to progression (surgery to progression) and the OS (time from surgery until death or last of follow-up news). As the analysis of the recurrence pattern after treatment was not part of the primary or secondary objectives of the STEMRI trial, but mostly dedicated to a subsequent ancillary study, the pattern of relapse has not been investigated in the present study and will be addressed in a future work.

Patient's selection

For the first part of the study, inclusion criteria concerned patients ≥ 18 years old, patients with performance scale ECOG 0–2, patients with life expectancy ≥ 3 months, patients who presented a radiological criterion of GBM and who had a surgical indication. Patients should also be affiliated to social security regimen and have voluntarily agreed to participate by giving written informed consent for this first part. For the second part of the study, the additional inclusion criterion was the presence of a histologically confirmed GBM. The exclusion criteria for the first part of the study concerned patients who were not allowed to perform an MRI, patients with non-contributive results after spectroscopic exam, pregnant or nursing patients, patients under law protection, patients who presented conditions that would interfere with cooperation with the trial requirements, and patients who presented medical, severe, or chronic biological or psychiatric conditions not allowing an enrolment in the study, according to the investigator's opinion. For the second part of the study, the exclusion criterion was receipt of the biological material in the laboratory more than 48 hours after surgery. As a consequence, 16 patients were lastly included in the second part of the trial and evaluable for the entire study (Table 1 and table S1).

Patients' imaging

MRI/MRSI acquisition

As described (76), data were acquired under the neurosurgeon supervision on a 3-T MRI system preceding surgery (ACHIEVA dStream, Philips Healthcare). A 32-channel phased-array receive coil was used. Three anatomical MRI sequences were then acquired (CHU Purpan). First, the anatomical MRI acquisition protocol included a three-dimensional (3D) T1-weighted sequence after 15-ml injection of gadolinium contrast [repetition time (TR)/echo time (TE) = 8/4 ms, fractional anisotropy (FA) = 8°, matrix = 165 × 241, 240 slices, 1 × 1 × 1 mm³ resolution], a FLAIR sequence [inversion time (TI)/TR/TE = 2400/8000/335 ms, FA = 90°, matrix = 200 × 256, 256 slices, resolution = 1 × 1 × 1 mm³], and a turbo-spin echo T2w sequence (TR/TE = 4130/80 ms, FA = 90°, matrix = 512 × 512, 43 slices, resolution = 0.5 × 0.5 × 3 mm³). Diffusion MRI sequence was also performed, and diffusion-weighted data were acquired in hyper-FLAIR regions with a single-shot echo-planar imaging (EPI) sequence [TR = 10 s, b value = 1000 s/mm², 15 directions (+1 b = 0), TE = 55 ms, matrix = 112 × 112, voxel size = 2 × 2 × 2 mm³, 60 slices]. Last, the 2D spectroscopy acquisition sequence (¹H-MRSI) was performed using a point-resolved spectroscopy acquisition (PRESS) over four slices covering the lesions. Matrix = 8 × 8, voxel size = 1 × 1 × 1 cm³, TR/TE = 1000/144

ms, two averages. Total acquisition time was around 45 to 50 min. Field of view was shifted away from brain-air interfaces when necessary.

MRI/MRSI data processing

Spectral processing (water subtraction, low-pass filtering, frequency-shift correction, baseline and phase correction, and curve fitting in the frequency domain) and the computation of Cho-to-NAA ratio index (CNI) map were performed with the Syngo MR B17 spectroscopy application (Siemens). ADC maps were computed using the Sisyphus Toolbox developed at our center (76), and the median values of ADC were then extracted at the biopsy location. Data were then processed according to our previous published studies (14, 15, 76).

Biopsy volume is defined by the needle size of 1.8 mm. The precision of the location is defined by (i) the spatial registration of the neuronavigation system (4 mm), (ii) the stability of the needle during extraction (approximately 2 mm), and (iii) the resolution of the anatomical image used for guidance (1 mm, leading to a precision of $1/\sqrt{12}$ mm at 1σ). Last, the biopsy lies in a volume of 680 mm³ at 1σ , or 2040 mm³ at 3σ , around the estimated location. Starting from the voxel corresponding to the estimated biopsy location, a morphological dilation was applied until the region of interest reached 2040 mm³ to take into account these uncertainties. This dilation was constrained in the manually drawn hyper-FLAIR region.

Tissue specimen surgical collection

For each patient, preoperative multimodal MRI was performed, and tumor localization was determined. During surgery, within the standard protocol set up in our hospital, a biopsy of the tumor was taken from the CE area, independently of the MRSI parameters, to be analyzed by the anatomopathology department for *MGMT* and *IDH* status determination.

As part of this clinical trial, as described in our recent study (76), the tumors were manually segmented according two preoperative MRI-visualized components: tumor bulk (CE and necrosis) and tumor edema (FLAIR) (Fig. 2, A and B). Hence, tumors were categorized into tumor functional zones, and segmentation in each zone (CE or FLAIR) was performed according to the CNI >2 or <2 regions (CNI+ or CNI–, respectively). The segmented tumor volumes, tractography, and computed maps were transferred to the neuronavigation planning system BrainLab iPlan, and the operating room BrainLab VectorVision Neuronavigation System (Nnav). Relative to surgery and biopsy extraction, to minimize brain shift, two biopsies were performed before resection according to the CNI >2 and <2 in the peritumoral edema regions using intraoperative MRI guidance. Resection was then performed according to the surgical standards of maximum safe resection of CE and more if possible, using neuronavigation and refined to take into account electrostimulation. During this CE resection, biopsies arising from CNI >2 and <2 areas were performed.

To sum up, for each patient, when possible according to surgical constraints and mapping results, it was planned to obtain a maximum of four different types of biopsies: FLAIR/CNI– (group 1); FLAIR/CNI+ (group 2); CE/CNI– (group 3); and CE/CNI+ (group 4). The correspondences between patients and collected samples are detailed in Table 2 and table S2.

Tissue specimen processing and culture

After extraction, biopsies were processed using our established protocol (38), and a small fraction of the sample was directly analyzed by flow cytometry to study the percentage of the GSC subpopulation at day 0 (biopsy GSC content or BGC%) over the total number of cells, as previously described (38). Next, another small fraction of each biopsy was set aside for RNA-seq analyses. Last, remaining cells were cultured as GSC-enriched NS in stem cell medium, as described in (38). In these restrictive conditions, only GSC can survive and form NS. All cultivated samples were observed daily under a microscope to check for the appearance of NS and thus report the TTN formation in days. Notably, the BGC% can be considered as a marker of malign stem-like cells' infiltration in the tumor biopsy and the TTN as a surrogate marker of tumor cell aggressiveness as shown in patients (61) and in xenografted mice (79).

MGMT and IDH status

IDH1/2 mutation and *MGMT* promoter methylation status were determined in all patients. To perform DNA extraction from formalin-fixed paraffin-embedded (FFPE) tissues, the Maxwell RSC DNA FFPE Kit (Promega) was used. DNA was quantified by fluorimetric assay with DNA Qubit, Broad Range (BR) Kit (Thermo Fisher Scientific), and purity was checked by NanoDrop ND-100 (Thermo Fisher Scientific).

We used pyrosequencing technology (PyroMark Q24, Qiagen) for real-time, sequence-based detection and quantification of sequence variants *IDH1/2*. Before pyrosequencing reaction, we made biotinylated-polymerase chain reaction (PCR) using a Pyromark PCR kit (Qiagen). Concerning biotinylated-PCR primers, for *IDH1* (NM_005896), we targeted the p.R132 codon and used the following pair of primers to generate a 74-bp amplicon size (*IDH1*-F-Biot: 5'-Biot-GGCTTGTGAGTGGATGGGTA-3', *IDH1*-R: 5'-GCCAACATGACTTACTTGATCC-3'). For *IDH2* (NM_002168), we targeted the p.R172 codon and used the following pair of primers to generate a 82-bp amplicon size (*IDH2*-F1: 5'-ATCCCACGCCTAGTCCCT-3'; *IDH2*-R1-Biot: 5'-Biot-CTCCACCCTGGCCTACCT-3'). Concerning the sequencing primers, because a single-stranded DNA template is required for pyrosequencing, the second strand must be removed. The pyrosequencing reaction have been performed on the purified biotinylated DNA template strand using the following sequencing primers: *IDH1*-S(R): 5'-GACTTACTTGATCCCCATA-3, *IDH2*-S1(F): 5'-AAGCCCATCACCAT-3'. As pyrosequencing uses sequential nucleotide injection, the nucleotides dispensation order allows quantification at all the chosen variant positions (*IDH1*: GAGCATCGATCTGACTA; *IDH2*: CGTCATGCAC). Last, the PyroMark Q24 Software 2.0 was used in allele quantification (AQ) mode for pyrogram analyses of listed *IDH1* variants: p.R132H, p.R132C, p.R132L, p.R132S, and p.R132G. For this, we used two different analysis sequences (AGCATGAHGACCTAT and AGCATGACNACCTAT) to call and detect the targeted mutation. To detect the listed *IDH2* variants: p.R172M, p.R172K, p.R172W, and p.R172G, we used two different sequences (GGCADGCACGCCAT and GGCDGGCAGCCCAT).

MGMT promoter methylation was assessed by pyrosequencing. Before pyrosequencing, bisulfite conversion was performed with the EZ DNA Methylation Kit (ZYMO RESEARCH) according to the supplier's recommendations as well as all the steps leading to *MGMT* pyrosequencing with the *MGMT* Pyro kit (Qiagen). The

MGMT Pyro Kit is used for quantitative measurement of methylation of four CpG sites in exon 1 of the human *MGMT* gene.

RNA-seq analysis of tumor bulk biopsies

RNA were isolated from frozen tissue material. The RNeasy lipid Tissue Mini Kit (Qiagen) was used, combined with Qiazol Reagent (Qiagen) to perform RNA extraction. RNA have been quantified by fluorimetric assay with the RNA Qubit Broad Range Kit (Thermo Fisher Scientific), and purity was checked by NanoDrop ND-100 (Thermo Fisher Scientific). The RNA quality have been checked with Bioanalyzer 2100 (Agilent Technologies) to get RIN (RNA integrity number) and to check for the absence of genomic DNA. Total RNA (100 ng) have been used for library preparation. Next-generation sequencing (NGS)-based RNA-seq have been performed by Helixio (Clermont-Ferrand, France) using the Illumina TruSeq Stranded Total RNA sample preparation with Ribo-Zero Gold depletion (Illumina) on a NextSeq 550 instrument according to the manufacturer's instructions (Illumina).

FastQ files were generated via Illumina bcl2fastq2 (version 2.20.0.422), then verified for quality (Fast-QC/MultiQC), aligned, and quantified using RNA-Seq by expectation maximization (RSEM) software package (RSEM 1.3.0, bowtie2.02.3.4) and the *Homo sapiens* transcriptome reference GRCh38 (v97) (80). Differential analysis of RNA-seq data (counts) at the gene level was performed using the DESeq2 (R package) with the recommended workflow (81). Adjusted *P* values (*q* values) were obtained as default by DESeq2 to control the global false discovery rate across all comparisons. Genes were considered differentially expressed if they had an adjusted *q* value <0.05 and a log₂ fold change ≥2. Pathway enrichment analyses were performed through successive analysis of the KEGG (C2_CP_KEGG), Hallmark (H), Reactome (C2_CP_Reactome) and GO BP (C5_GO_BP) databases with the AutoCompare SES tool. Last, the obtained scores by samples for each group (FLAIR/CNI-, FLAIR/CNI+, CE/CNI-, CE/CNI+, CNI-, CNI+, CE, and FLAIR) were compared using a *t* test. Significant signatures were those with a *P* value <0.05. The different databases and tools are available from Fred's Softwares at <https://sites.google.com/site/fredsoftwares/products> (82).

Molecular subtype of each biopsy was determined according to either Verhaak (34) or Wang (35) classification. For Verhaak classification, the Simple GBM Subclassifier online tool (www.semml.ucla.edu/coppola-lab/simple-glioblastoma-subclassifier) was used to classify samples into four molecular subgroups (Ne, Neural; PN, proneural; Mes, Mesenchymal; C, Classical), while for Wang classification, the Gliovis data portal and the SubtypeME tool (<http://gliovis.bioinfo.cnio.es>) (37) were used to classify biopsies into three tumor-specific subtypes: PN, Mes, and CL.

Flow cytometry

Direct immunofluorescence assay was performed by FACS as described (33, 38). The antibodies used were A2B5-allophycocyanin (APC) and O4-phycoerythrin (PE) (Miltenyi Biotec), CD133/2-PE, CD15-Peridinin-chlorophyll (PerCP), NOTCH1-PerCP, NANOG-PE, Nestin-fluorescein, ITGβ8-APC, and Sox2-APC (R&D Systems); glial fibrillary acidic protein-PE (Millipore); and TUJ1-Alexa Fluor 488, KI67-PE cyanin7 (PECy7), and CD44-PECy7 (BD Biosciences) and ITGa6-PE (Thermo Fisher Scientific).

For marker expression results, specific fluorescence index and gating strategy were previously described (38).

Clonogenic assays

NS from different patients and localizations were seeded in 96-well plates (500 cells per well, 16 wells per condition). After 24 hours, cells were treated or not with different doses of gamma rays (2 to 10 Gy). Then, 8 to 15 days after IR, the number of NS per well with more than 50 cells was measured. The untreated condition allowed us to measure the clonogenic potential of each cell lines, as the percentages of GSC cells able to generate secondary NS. For IR conditions, the best-fit survival curves were generated according to the linear quadratic model and the MID calculated, as already detailed (83).

Orthotopic xenografts

Nude mice were used in accordance to a protocol (APAFIS#7660-2016110818123504 v2) reviewed and approved by the Institutional Animal Care and Use Committee of Région Midi-Pyrénées (France). Orthotopic human GBM xenografts were established in 4- to 6-week-old female nude mice (Janvier Labs) as previously described (38). Briefly, mice (three to seven per group) received a stereotaxically guided injection of 2.5×10^5 cells resuspended in 5 μ l of Dulbecco's modified Eagle's medium-F12. Survival curves were established, and mice were euthanized at the appearance of neurological signs. Excised brains were collected for subsequent immunohistochemistry analysis of the tumor and determination of the tumor penetrance rate.

Immunohistochemistry

Immunohistochemistry was performed, as previously described (33), on paraffin-embedded sections (5 μ m) of excised brains of xenografted mice. The primary antibody used was mouse anti-Nestin (Millipore MAB5326).

Statistical analysis

In regard to the exploratory nature of this pilot study, no formal sample size calculation was performed and it was planned to include 16 eligible patients. Data were described using frequencies and percentages for qualitative variables and using median and range or mean and SEM for quantitative variables. Comparisons between pairs of biopsies CNI+ versus CNI- were performed using the Wilcoxon signed-rank test for paired data for quantitative variables and the McNemar test for qualitative variables. OS and PFS were estimated using the Kaplan-Meier method. Univariate analyses were performed using log-rank test for qualitative variables and a Cox proportional hazard model for quantitative variables. All statistical tests were two sided, and a *P* value <0.05 was considered as statistically significant. Statistical analysis was performed using Stata software version 16.

Supplementary Materials

This PDF file includes:

Figs. S1 to S8

Tables S1 to S12

REFERENCES AND NOTES

1. M. Weller, M. van den Bent, K. Hopkins, J. C. Tonn, R. Stupp, A. Falini, E. Cohen-Jonathan-Moyal, D. Frappaz, R. Henriksson, C. Balana, O. Chinot, Z. Ram, G. Reifenberger, R. Soffietti, W. Wick, EANO guideline for the diagnosis and treatment of anaplastic gliomas and glioblastoma. *Lancet Oncol.* **15**, e395–e403 (2014).
2. R. Stupp, S. Taillibert, A. Kanner, W. Read, D. M. Steinberg, B. Lhermitte, S. Toms, A. Idbaih, M. S. Ahluwalia, K. Fink, F. Di Meco, F. Lieberman, J.-J. Zhu, G. Stragliotto, D. D. Tran, S. Brem, A. F. Hottinger, E. D. Kirson, G. Lavy-Shahaf, U. Weinberg, C.-Y. Kim, S.-H. Paek, G. Nicholas, J. Bruna, H. Hirte, M. Weller, Y. Palti, M. E. Hegi, Z. Ram, Effect of Tumor-Treating Fields Plus Maintenance Temozolomide vs Maintenance Temozolomide Alone on Survival in Patients With Glioblastoma: A Randomized Clinical Trial. *JAMA* **318**, 2306–2316 (2017).
3. K. Mitchell, K. Troike, D. J. Silver, J. D. Lathia, The evolution of the cancer stem cell state in glioblastoma: emerging insights into the next generation of functional interactions. *Neuro Oncol.* **23**, 199–213 (2021).
4. R. C. Gimple, K. Yang, M. E. Halbert, S. Agnihotri, J. N. Rich, Brain cancer stem cells: resilience through adaptive plasticity and hierarchical heterogeneity. *Nat. Rev. Cancer* **22**, 497–514 (2022).
5. R. M. Gangemi, F. Griffero, D. Marubbi, M. Perera, M. C. Capra, P. Malatesta, G. L. Ravetti, G. L. Zona, A. Daga, G. Corte, SOX2 silencing in glioblastoma tumor-initiating cells causes stop of proliferation and loss of tumorigenicity. *Stem Cells* **27**, 40–48 (2009).
6. P. Brescia, B. Ortensi, L. Fornasari, D. Levi, G. Broggi, G. Pelicci, CD133 Is Essential for Glioblastoma Stem Cell Maintenance. *Stem Cells* **31**, 857–869 (2013).
7. Y. Matsuda, T. Ishiwata, H. Yoshimura, M. Hagio, T. Arai, Inhibition of nestin suppresses stem cell phenotype of glioblastomas through the alteration of post-translational modification of heat shock protein HSPA8/HSC71. *Cancer Lett.* **357**, 602–611 (2015).
8. K. L. Ligon, E. Huillard, S. Mehta, S. Kesari, H. Liu, J. A. Alberta, R. M. Bachoo, M. Kane, D. N. Louis, R. A. DePinho, D. J. Anderson, C. D. Stiles, D. H. Rowitch, Olig2-Regulated Lineage-Restricted Pathway Controls Replication Competence in Neural Stem Cells and Malignant Glioma. *Neuron* **53**, 503–517 (2007).
9. A. Tchoghandjian, N. Baeza, C. Colin, M. Cayre, P. Metellus, C. Beclin, L. Ouafik, D. Figarella-Branger, A2B5 cells from human glioblastoma have cancer stem cell properties. *Brain Pathol.* **20**, 211–221 (2010).
10. J. D. Lathia, J. Gallagher, J. M. Heddleston, J. Wang, C. E. Eyler, J. Macswords, Q. Wu, A. Vasanji, R. E. McLendon, A. B. Hjelmeland, J. N. Rich, Integrin alpha 6 regulates glioblastoma stem cells. *Cell Stem Cell* **6**, 421–432 (2010).
11. R. C. Gimple, S. Bhargava, D. Dixit, J. N. Rich, Glioblastoma stem cells: lessons from the tumor hierarchy in a lethal cancer. *Genes Dev.* **33**, 591–609 (2019).
12. L. S. Hu, A. Hawkins-Daarud, L. Wang, J. Li, K. R. Swanson, Imaging of intratumoral heterogeneity in high-grade glioma. *Cancer Lett.* **477**, 97–106 (2020).
13. M. E. Laino, R. Young, K. Beal, S. Haque, Y. Mazaheri, G. Corrias, A. G. Bitencourt, S. Karimi, S. B. Thakur, Magnetic resonance spectroscopic imaging in gliomas: clinical diagnosis and radiotherapy planning. *BJR Open* **2**, 20190026 (2020).
14. A. Laprie, I. Catalaa, E. Cassol, T. R. McKnight, D. Berchery, D. Marre, J. M. Bachaud, I. Berry, E. C. Moyal, Proton magnetic resonance spectroscopic imaging in newly diagnosed glioblastoma: predictive value for the site of postradiotherapy relapse in a prospective longitudinal study. *Int. J. Radiat. Oncol. Biol. Phys.* **70**, 773–781 (2008).
15. A. Deviers, S. Ken, T. Filleron, B. Rowland, A. Laruelo, I. Catalaa, V. Lubrano, P. Celsis, I. Berry, G. Moggicato, E. Cohen-Jonathan Moyal, A. Laprie, Evaluation of the lactate-to-N-acetyl-aspartate ratio defined with magnetic resonance spectroscopic imaging before radiation therapy as a new predictive marker of the site of relapse in patients with glioblastoma multiforme. *Int. J. Radiat. Oncol. Biol. Phys.* **90**, 385–393 (2014).
16. I. Park, G. Tamai, M. C. Lee, C. F. Chuang, S. M. Chang, M. S. Berger, S. J. Nelson, A. Pirzkall, Patterns of recurrence analysis in newly diagnosed glioblastoma multiforme after three-dimensional conformal radiation therapy with respect to pre-radiation therapy magnetic resonance spectroscopic findings. *Int. J. Radiat. Oncol. Biol. Phys.* **69**, 381–389 (2007).
17. F. W. Crawford, I. S. Khayal, C. McGue, S. Saraswathy, A. Pirzkall, S. Cha, K. R. Lamborn, S. M. Chang, M. S. Berger, S. J. Nelson, Relationship of pre-surgery metabolic and physiological MR imaging parameters to survival for patients with untreated GBM. *J. Neurooncol* **91**, 337–351 (2009).
18. Y. Li, J. M. Lupo, R. Parvataneni, K. R. Lamborn, S. Cha, S. M. Chang, S. J. Nelson, Survival analysis in patients with newly diagnosed glioblastoma using pre- and postradiotherapy MR spectroscopic imaging. *Neuro Oncol.* **15**, 607–617 (2013).
19. S. Saraswathy, F. W. Crawford, K. R. Lamborn, A. Pirzkall, S. Chang, S. Cha, S. J. Nelson, Evaluation of MR markers that predict survival in patients with newly diagnosed GBM prior to adjuvant therapy. *J. Neurooncol* **91**, 69–81 (2009).
20. Y. Cui, W. Zeng, H. Jiang, X. Ren, S. Lin, Y. Fan, Y. Liu, Y. Zhao, Higher Cho/NAA Ratio in Postoperative Peritumoral Edema Zone Is Associated With Earlier Recurrence of Glioblastoma. *Front. Neurol.* **11**, 592155 (2020).

21. P. Talati, M. El-Abtah, D. Kim, J. Dietrich, M. Fu, M. Wenke, J. He, S. N. Natheir, M. Vangel, O. Rapalino, A. Vaynrub, I. Arrillaga-Romany, D. A. Forst, Y.-F. Yen, O. Andronesi, J. Kalpathy-Cramer, B. Rosen, T. T. Batchelor, R. G. Gonzalez, E. R. Gerstner, E.-M. Ratai, MR spectroscopic imaging predicts early response to anti-angiogenic therapy in recurrent glioblastoma. *Neuro-Oncol. Adv.* **3**, vdab060 (2021).
22. A. Pirzkall, X. Li, J. Oh, S. Chang, M. S. Berger, D. A. Larson, L. J. Verhey, W. P. Dillon, S. J. Nelson, 3D MRSI for resected high-grade gliomas before RT: tumor extent according to metabolic activity in relation to MRI. *Int. J. Radiat. Oncol. Biol. Phys.* **59**, 126–137 (2004).
23. T. R. McKnight, M. H. von dem Bussche, D. B. Vigneron, Y. Lu, M. S. Berger, M. W. McDermott, W. P. Dillon, E. E. Graves, A. Pirzkall, S. J. Nelson, Histopathological validation of a three-dimensional magnetic resonance spectroscopy index as a predictor of tumor presence. *J. Neurosurg.* **97**, 794–802 (2002).
24. E. C. Moyal, A. Laprie, M. Delannes, M. Poulblanc, I. Catalaa, F. Dalenc, D. Berchery, J. Sabatier, P. Bousquet, P. De Porre, B. Alaux, C. Toulas, Phase I trial of tipifarnib (R115777) concurrent with radiotherapy in patients with glioblastoma multiforme. *Int. J. Radiat. Oncol. Biol. Phys.* **68**, 1396–1401 (2007).
25. S. J. Price, A. M. H. Young, W. J. Scotton, J. Ching, L. A. Mohsen, N. R. Boonzaier, V. C. Lupson, J. R. Griffiths, M. A. McLean, T. J. Larkin, Multimodal MRI can identify perfusion and metabolic changes in the invasive margin of glioblastomas. *J. Magn. Reson. Imaging* **43**, 487–494 (2016).
26. J. Chen, Y. Li, T.-S. Yu, R. M. McKay, D. K. Burns, S. G. Kernie, L. F. Parada, A restricted cell population propagates glioblastoma growth after chemotherapy. *Nature* **488**, 522–526 (2012).
27. X. P. Xie, D. R. Laks, D. Sun, M. Ganbold, Z. Wang, A. M. Pedraza, T. Bale, V. Tabar, C. Brennan, X. Zhou, L. F. Parada, Quiescent human glioblastoma cancer stem cells drive tumor initiation, expansion, and recurrence following chemotherapy. *Dev. Cell* **57**, 32–46.e8 (2022).
28. J. S. Cordova, H.-K. G. Shu, Z. Liang, S. S. Gurbani, L. A. D. Cooper, C. A. Holder, J. J. Olson, B. Kairdolf, E. Schreiber, S. G. Neill, C. G. Hadjipanayis, H. Shim, Whole-brain spectroscopic MRI biomarkers identify infiltrating margins in glioblastoma patients. *Neuro Oncol.* **18**, 1180–1189 (2016).
29. V. Mlynarik, C. Cudalbu, V. Clement, D. Marino, I. Radovanovic, R. Gruetter, In vivo metabolic profiling of glioma-initiating cells using proton magnetic resonance spectroscopy at 14.1 Tesla. *NMR Biomed.* **25**, 506–513 (2012).
30. M. Lai, I. Vassallo, B. Lanz, C. Poiry-Yamate, M.-F. Hamou, C. Cudalbu, R. Gruetter, M. E. Hegi, In vivo characterization of brain metabolism by ¹H MRS, ¹³C MRS and ¹⁸FDG PET reveals significant glucose oxidation of invasively growing glioma cells. *Int. J. Cancer* **143**, 127–138 (2018).
31. D. N. Louis, A. Perry, P. Wesseling, D. J. Brat, I. A. Cree, D. Figarella-Branger, C. Hawkins, H. K. Ng, S. M. Pfister, G. Reifenberger, R. Soffietti, A. von Deimling, D. W. Ellison, The 2021 WHO Classification of Tumors of the Central Nervous System: a summary. *Neuro Oncol.* **23**, 1231–1251 (2021).
32. J. Anido, A. Saez-Borderias, A. Gonzalez-Junca, L. Rodon, G. Folch, M. A. Carmona, R. M. Prieto-Sanchez, I. Barba, E. Martinez-Saez, L. Prudkin, I. Cuartas, C. Raventos, F. Martinez-Ricarte, M. A. Poca, D. Garcia-Dorado, M. M. Lahn, J. M. Yingling, J. Rodon, J. Sahuquillo, J. Baselga, J. Seoane, TGF- β Receptor Inhibitors Target the CD44high/Id1high Glioma-Initiating Cell Population in Human Glioblastoma. *Cancer Cell* **18**, 655–668 (2010).
33. L. Malric, S. Monferran, C. Delmas, F. Arnauduc, P. Dahan, S. Boyrie, P. Deshors, V. Lubrano, D. F. Da Mota, J. Gilhodes, T. Filleron, A. Siegfried, S. Evrard, A. Kowalski-Chauvel, E. C. Moyal, C. Toulas, A. Lemarie, Inhibiting Integrin $\beta 8$ to Differentiate and Radiosensitize Glioblastoma-Initiating Cells. *Mol. Cancer Res.* **17**, 384–397 (2019).
34. R. G. Verhaak, K. A. Hoadley, E. Purdom, V. Wang, Y. Qi, M. D. Wilkerson, C. R. Miller, L. Ding, T. Golub, J. P. Mesirov, G. Alexe, M. Lawrence, M. O'Kelly, P. Tamayo, B. A. Weir, S. Gabriel, W. Winckler, S. Gupta, L. Jakkula, H. S. Feiler, J. G. Hodgson, C. D. James, J. N. Sarkaria, C. Brennan, A. Kahn, P. T. Spellman, R. K. Wilson, T. P. Speed, J. W. Gray, M. Meyerson, G. Getz, C. M. Perou, D. N. Hayes, N., Integrated genomic analysis identifies clinically relevant subtypes of glioblastoma characterized by abnormalities in PDGFRA, IDH1, EGFR, and NF1. *Cancer Cell* **17**, 98–110 (2010).
35. Q. Wang, B. Hu, X. Hu, H. Kim, M. Squatrito, L. Scarpace, A. C. deCarvalho, S. Lyu, P. Li, Y. Li, F. Barthel, H. J. Cho, Y. H. Lin, N. Satani, E. Martinez-Ledesma, S. Zheng, E. Chang, C. G. Sauve, A. Olar, Z. D. Lan, G. Finocchiaro, J. J. Phillips, M. S. Berger, K. R. Gabrusiewicz, G. Wang, E. Eskilsson, J. Hu, T. Mikkelsen, R. A. DePinho, F. Muller, A. B. Heimberger, E. P. Sulman, D. H. Nam, R. G. W. Verhaak, Tumor Evolution of Glioma-Intrinsic Gene Expression Subtypes Associates with Immunological Changes in the Microenvironment. *Cancer Cell.* **32**, 42–56.e6 (2017).
36. O. Eidel, J.-O. Neumann, S. Burth, P. J. Kieslich, C. Jungk, F. Sahn, P. Kickingeder, K. Kiening, A. Unterberg, W. Wick, H.-P. Schlemmer, M. Bendszus, A. Radbruch, Automatic Analysis of Cellularity in Glioblastoma and Correlation with ADC Using Trajectory Analysis and Automatic Nuclei Counting. *PLOS ONE* **11**, e0160250 (2016).
37. R. L. Bowman, Q. Wang, A. Carro, R. G. W. Verhaak, M. Squatrito, GlioVis data portal for visualization and analysis of brain tumor expression datasets. *Neuro Oncol.* **19**, 139–141 (2017).
38. P. Dahan, J. Martinez Gala, C. Delmas, S. Monferran, L. Malric, D. Zentkowski, V. Lubrano, C. Toulas, E. Cohen-Jonathan Moyal, A. Lemarie, Ionizing radiations sustain glioblastoma cell dedifferentiation to a stem-like phenotype through survivin: possible involvement in radioresistance. *Cell Death Dis.* **5**, e1543 (2014).
39. F. Padelli, F. Mazzi, A. Erbetta, L. Chiapparini, F. M. Doniselli, S. Palermo, D. Aquino, M. G. Bruzzone, V. Cuccarini, In vivo brain MR spectroscopy in gliomas: clinical and pre-clinical chances. *Clin Transl Imag.* **10**, 495–515 (2022).
40. F. Hesse, A. J. Wright, V. Somai, F. Bulat, F. Kreis, K. M. Brindle, Imaging Glioblastoma Response to Radiotherapy Using ²H Magnetic Resonance Spectroscopy Measurements of Fumarate Metabolism. *Cancer Res.* **82**, 3622–3633 (2022).
41. M. Law, S. Yang, H. Wang, J. S. Babb, G. Johnson, S. Cha, E. A. Knopp, D. Zagzag, Glioma grading: sensitivity, specificity, and predictive values of perfusion MR imaging and proton MR spectroscopic imaging compared with conventional MR imaging. *Am. J. Neuroradiol.* **24**, 1989–1998 (2003).
42. I. Sidibe, F. Tensaouti, J. Gilhodes, B. Cabarrou, T. Filleron, F. Desmoulin, S. Ken, G. Noël, G. Truc, M. P. Sunyach, M. Charissoux, N. Magné, J.-A. Lotterie, M. Roques, P. Péran, E. Cohen-Jonathan Moyal, A. Laprie, Pseudoprogression in GBM versus true progression in patients with glioblastoma: A multiapproach analysis. *Radiother. Oncol.* **181**, 109486 (2023).
43. Q.-S. Zeng, C.-F. Li, H. Liu, J.-H. Zhen, D.-C. Feng, Distinction Between Recurrent Glioma and Radiation Injury Using Magnetic Resonance Spectroscopy in Combination With Diffusion-Weighted Imaging. *Int. J. Radiat. Oncol. Biol. Phys.* **68**, 151–158 (2007).
44. T. Kazda, M. Bulik, P. Pospisil, R. Lakomy, M. Smrcka, P. Slampa, R. Jancalek, Advanced MRI increases the diagnostic accuracy of recurrent glioblastoma: Single institution thresholds and validation of MR spectroscopy and diffusion weighted MR imaging. *NeuroImage: Clinical.* **11**, 316–321 (2016).
45. A. E. Elias, R. C. Carlos, E. A. Smith, D. Frechtling, B. George, P. Maly, P. C. Sundgren, MR Spectroscopy Using Normalized and Non-normalized Metabolite Ratios for Differentiating Recurrent Brain Tumor from Radiation Injury. *Acad. Radiol.* **18**, 1101–1108 (2011).
46. M. Muruganandham, P. P. Clerkin, B. J. Smith, C. M. Anderson, A. Morris, A. A. Capizzano, V. Magnotta, S. M. McGuire, M. C. Smith, J. E. Bayouth, J. M. Buatti, 3-Dimensional Magnetic Resonance Spectroscopic Imaging at 3 Tesla for Early Response Assessment of Glioblastoma Patients During External Beam Radiation Therapy. *Int. J. Radiat. Oncol. Biol. Phys.* **90**, 181–189 (2014).
47. F. Tensaouti, F. Desmoulin, J. Gilhodes, M. Roques, S. Ken, J.-A. Lotterie, G. Noël, G. Truc, M.-P. Sunyach, M. Charissoux, N. Magné, V. Lubrano, P. Péran, E. Cohen-Jonathan Moyal, A. Laprie, Is pre-radiotherapy metabolic heterogeneity of glioblastoma predictive of progression-free survival? *Radiother. Oncol.* **183**, 109665 (2023).
48. M. Castellán, A. Guarnieri, A. Fujimura, F. Zanconato, G. Battilana, T. Panciera, H. L. Sladitschek, P. Contessotto, A. Citron, A. Grilli, O. Romano, S. Bicciato, M. Fassan, E. Porcù, A. Rosato, M. Cordenonsi, S. Piccolo, Single-cell analyses reveal YAP/TAZ as regulators of stemness and cell plasticity in Glioblastoma. *Nat. Cancer.* **2**, 174–188 (2021).
49. A. Kowalski-Chauvel, V. Gouaze-Anderson, L. Baricault, E. Martin, C. Delmas, C. Toulas, E. Cohen-Jonathan-Moyal, C. Seva, Alpha6-Integrin Regulates FGFR1 Expression through the ZEB1/YAP1 Transcription Complex in Glioblastoma Stem Cells Resulting in Enhanced Proliferation and Stemness. *Cancer* **11**, E406 (2019).
50. V. Clement, P. Sanchez, N. de Tribolet, I. Radovanovic, A. R. Altaba, HEDGEHOG-GLI1 signaling regulates human glioma growth, cancer stem cell self-renewal, and tumorigenicity. *Curr. Biol.* **17**, 165–172 (2007).
51. J. Wang, H. Wang, Z. Li, Q. Wu, J. D. Lathia, R. E. McLendon, A. B. Hjelmeland, J. N. Rich, c-Myc is required for maintenance of glioma cancer stem cells. *PLOS ONE* **3**, e3769 (2008).
52. X. Fan, L. Khaki, T. S. Zhu, M. E. Soules, C. E. Talsma, N. Gul, C. Koh, J. Zhang, Y. M. Li, J. Maciaczyk, G. Nikkha, F. Dimco, S. Piccirillo, A. L. Vescevi, C. G. Eberhart, NOTCH pathway blockade depletes CD133-positive glioblastoma cells and inhibits growth of tumor neurospheres and xenografts. *Stem Cells* **28**, 5–16 (2010).
53. E. Vlashi, C. Lagadeç, L. Vergnes, T. Matsutani, K. Masui, M. Poulou, R. Popescu, L. Della Donna, P. Evers, C. Dekmezian, K. Reue, H. Christofk, P. S. Mischel, F. Pajonk, Metabolic state of glioma stem cells and nontumorigenic cells. *Proc. Natl. Acad. Sci. U.S.A.* **108**, 16062–16067 (2011).
54. M. Janiszewska, M. L. Suva, N. Riggi, R. H. Houtkooper, J. Auwerx, V. Clement-Schatlo, I. Radovanovic, E. Rheinbay, P. Provero, I. Stamenkovic, Imp2 controls oxidative phosphorylation and is crucial for preserving glioblastoma cancer stem cells. *Genes Dev.* **26**, 1926–1944 (2012).
55. K. Kuramoto, M. Yamamoto, S. Suzuki, T. Sanomachi, K. Togashi, S. Seino, C. Kitanaka, M. Okada, Verteporfin inhibits oxidative phosphorylation and induces cell death specifically in glioma stem cells. *FEBS J.* **287**, 2023–2036 (2020).

56. B. Qiu, D. Zhang, J. Tao, X. Tie, A. Wu, Y. Wang, Human brain glioma stem cells are more invasive than their differentiated progeny cells in vitro. *J. Clin. Neurosci.* **19**, 130–134 (2011).
57. S. M. Turaga, J. D. Lathia, Adhering towards tumorigenicity: altered adhesion mechanisms in glioblastoma cancer stem cells. *CNS Oncol.* **5**, 251–259 (2016).
58. P. Ruiz-Ontanon, J. L. Orgaz, B. Aldaz, A. Elosegui-Artola, J. Martino, M. T. Berciano, J. A. Montero, L. Grande, L. Nogueira, S. Diaz-Moralli, A. Esparis-Ogando, A. Vazquez-Barquero, M. Lafarga, A. Pandiella, M. Cascante, V. Segura, J. A. Martinez-Climent, V. Sanz-Moreno, J. L. Fernandez-Luna, Cellular plasticity confers migratory and invasive advantages to a population of glioblastoma-initiating cells that infiltrate peritumoral tissue. *Stem Cells* **31**, 1075–1085 (2013).
59. C. Cudalbu, P. Bady, M. Lai, L. Xin, O. Gusyatiner, M.-F. Hamou, M. Lepore, J.-P. Brouland, R. T. Daniel, A. F. Hottinger, M. E. Hegi, Metabolic and transcriptomic profiles of glioblastoma invasion revealed by comparisons between patients and corresponding orthotopic xenografts in mice. *Acta Neuropathol. Commun.* **9**, 133 (2021).
60. S. Grande, A. Palma, L. Ricci-Vitiani, A. M. Luciani, M. Buccarelli, M. Biffoni, A. Molinari, A. Calcabrini, E. D'Amore, L. Guidoni, R. Pallini, V. Viti, A. Rosi, Metabolic Heterogeneity Evidenced by MRS among Patient-Derived Glioblastoma Multiforme Stem-Like Cells Accounts for Cell Clustering and Different Responses to Drugs. *Stem Cells Int.* **2018**, 1–16 (2018).
61. D. R. Laks, M. Masterman-Smith, K. Visnyei, B. Angenieux, N. M. Orozco, I. Foran, W. H. Yong, H. V. Vinters, L. M. Liau, J. A. Lazareff, P. S. Mischel, T. F. Cloughesy, S. Horvath, H. I. Kornblum, Neurosphere formation is an independent predictor of clinical outcome in malignant glioma. *Stem Cells* **27**, 980–987 (2009).
62. Q. G. D'Alessandris, M. Biffoni, M. Martini, D. Runci, M. Buccarelli, T. Cenci, M. Signore, L. Stancato, A. Olivi, R. De Maria, L. M. Larocca, L. Ricci-Vitiani, R. Pallini, The clinical value of patient-derived glioblastoma tumospheres in predicting treatment response. *Neuro Oncol.* **19**, 1097–1108 (2017).
63. P. C. Jayakrishnan, E. H. Venkat, G. M. Ramachandran, K. K. Kesavapisharady, S. N. Nair, B. Bharathan, N. Radhakrishnan, S. Gopala, In vitro neurosphere formation correlates with poor survival in glioma. *IUBMB Life* **71**, 244–253 (2019).
64. R. Pallini, L. Ricci-Vitiani, G. L. Banna, M. Signore, D. Lombardi, M. Todaro, G. Stassi, M. Martini, G. Maira, L. M. Larocca, R. De Maria, Cancer stem cell analysis and clinical outcome in patients with glioblastoma multiforme. *Clin. Cancer Res.* **14**, 8205–8212 (2008).
65. M. Zhang, T. Song, L. Yang, R. Chen, L. Wu, Z. Yang, J. Fang, Nestin and CD133: valuable stem cell-specific markers for determining clinical outcome of glioma patients. *J. Exp. Clin. Cancer Res.* **27**, 85–85 (2008).
66. F. Zeppernick, R. Ahmadi, B. Campos, C. Dictus, B. M. Helmke, N. Becker, P. Lichter, A. Unterberg, B. Radlwimmer, C. C. Herold-Mende, Stem cell marker CD133 affects clinical outcome in glioma patients. *Clin. Cancer Res.* **14**, 123–129 (2008).
67. B. Wu, C. Sun, F. Feng, M. Ge, L. Xia, Do relevant markers of cancer stem cells CD133 and Nestin indicate a poor prognosis in glioma patients? A systematic review and meta-analysis. *J. Exp. Clin. Cancer Res.* **34**, 44 (2015).
68. J. Zhang, L. Chen, L. Han, Z. Shi, J. Zhang, P. Pu, C. Kang, EZH2 is a negative prognostic factor and exhibits pro-oncogenic activity in glioblastoma. *Cancer Lett.* **356**, 929–936 (2015).
69. J. Li, Y. Cui, G. Gao, Z. Zhao, H. Zhang, X. Wang, Notch1 is an independent prognostic factor for patients with glioma. *J. Surg. Oncol.* **103**, 813–817 (2011).
70. P. Karschnia, M. A. Vogelbaum, M. van den Bent, D. P. Cahill, L. Bello, Y. Narita, M. S. Berger, M. Weller, J.-C. Tonn, Evidence-based recommendations on categories for extent of resection in diffuse glioma. *Eur. J. Cancer* **149**, 23–33 (2021).
71. Y. M. Li, D. Suki, K. Hess, R. Sawaya, The influence of maximum safe resection of glioblastoma on survival in 1229 patients: Can we do better than gross-total resection? *JNS.* **124**, 977–988 (2016).
72. A. M. Molinaro, S. Hervey-Jumper, R. A. Morshed, J. Young, S. J. Han, P. Chunduru, Y. Zhang, J. J. Phillips, A. Shai, M. Lafontaine, J. Crane, A. Chandra, P. Flanagan, A. Jahangiri, G. Cioffi, Q. Ostrom, J. E. Anderson, C. Badve, J. Barnholtz-Sloan, A. E. Sloan, B. J. Erickson, P. A. Decker, M. L. Kosel, D. LaChance, J. Eckerl-Passow, R. Jenkins, J. Villanueva-Meyer, T. Rice, M. Wrensch, J. K. Wiencke, N. A. Oberheim Bush, J. Taylor, N. Butowski, M. Prados, J. Clarke, S. Chang, E. Chang, M. Agbi, P. Theodosopoulos, M. McDermott, M. S. Berger, Association of Maximal Extent of Resection of Contrast-Enhanced and Non-Contrast-Enhanced Tumor With Survival Within Molecular Subgroups of Patients With Newly Diagnosed Glioblastoma. *Oncologia* **6**, 495 (2020).
73. A. F. Haddad, J. S. Young, R. A. Morshed, M. S. Berger, FLAIRctomy: Resecting beyond the Contrast Margin for Glioblastoma. *Brain Sci.* **12**, 544 (2022).
74. A. Laprie, G. Noel, L. Chaltiel, G. Truc, M.-P. Sunyach, M. Charissoux, N. Magne, P. Auberdiac, J. Biau, S. Ken, F. Tensaouti, J. Khalifa, I. Sidibe, F.-E. Roux, L. Vieillelveigne, I. Catalaa, S. Boetto, U.-C. Emmanuelle, S. Supiot, V. Bernier, T. Filleron, M. Mounier, M. Poulblanc, P. Olivier, J.-P. Delord, E. Cohen-Jonathan-Moyal, Randomized phase III trial of metabolic imaging-guided dose escalation of radio-chemotherapy in patients with newly diagnosed glioblastoma (SPECTRO GLIO trial). *Neuro Oncol.* **noad119**, (2023).
75. K. Ramesh, E. A. Mellon, S. S. Gurbani, B. D. Weinberg, E. Schreiber, S. A. Sheriff, M. Goryawala, M. De Le Fuente, B. R. Eaton, J. Zhong, A. D. Voloschin, S. Sengupta, E. M. Dunbar, M. Holdhoff, P. B. Barker, A. A. Maudsley, L. R. Kleinberg, H. Shim, H.-K. G. Shu, A multi-institutional pilot clinical trial of spectroscopic MRI-guided radiation dose escalation for newly diagnosed glioblastoma. *Neuro-Oncology. Advances* **4**, vdc006 (2022).
76. T. Duval, J.-A. Lotterie, A. Lemarie, C. Delmas, F. Tensaouti, E. C.-J. Moyal, V. Lubrano, Glioblastoma Stem-like Cell Detection Using Perfusion and Diffusion MRI. *Cancer* **14**, 2803 (2022).
77. S. Monferran, N. Skuli, C. Delmas, G. Favre, J. Bonnet, E. Cohen-Jonathan-Moyal, C. Toulas, Alpha5beta3 and alpha5beta5 integrins control glioma cell response to ionising radiation through ILK and RhoB. *Int. J. Cancer* **123**, 357–364 (2008).
78. R. Stupp, W. P. Mason, M. J. van den Bent, M. Weller, B. Fisher, M. J. Taphoorn, K. Belanger, A. A. Brandes, C. Marosi, U. Bogdahn, J. Curschmann, R. C. Janzer, S. K. Ludwin, T. Gorlia, A. Allgeier, D. Lacombe, J. G. Cairncross, E. Eisenhauer, R. O. Mirimanoff, Radiotherapy plus concomitant and adjuvant temozolomide for glioblastoma. *N. Engl. J. Med.* **352**, 987–996 (2005).
79. C. Cusulin, C. Chesnelong, P. Bose, M. Bilenky, K. Kopciuk, J. A. Chan, J. G. Cairncross, S. J. Jones, M. A. Marra, H. A. Luchman, S. Weiss, Precursor States of Brain Tumor Initiating Cell Lines Are Predictive of Survival in Xenografts and Associated with Glioblastoma Subtypes. *Stem Cell Rep.* **5**, 1–9 (2015).
80. B. Li, C. N. Dewey, RSEM: accurate transcript quantification from RNA-Seq data with or without a reference genome. *BMC Bioinform.* **12**, 323 (2011).
81. M. I. Love, W. Huber, S. Anders, Moderated estimation of fold change and dispersion for RNA-seq data with DESeq2. *Genome Biol.* **15**, 550 (2014).
82. M. Tosolini, C. Algans, F. Pont, B. Ycart, J.-J. Fournié, Large-scale microarray profiling reveals four stages of immune escape in non-Hodgkin lymphomas. *Oncotargets. Ther.* **5**, e1188246 (2016).
83. I. Ader, C. Toulas, F. Dalenc, C. Delmas, J. Bonnet, E. Cohen-Jonathan, G. Favre, RhoB controls the 24 kDa FGF-2-induced radioresistance in HeLa cells by preventing post-mitotic cell death. *Oncogene* **21**, 5998–6006 (2002).

Acknowledgments: We would like to thank E. Uro-Coste, M. Courtade-Saidi, and S. Evrard at the CHU Toulouse–IUCT–Oncopole Anatomopathology service, as well as A. Fabre at the IUCT Clinical Trials department and A. Hagimont (CRCT) for technical advices. We would also thank the CRCT Technology Cluster, the CREFRE animal facility in Toulouse, INSERM, and the Association pour la Recherche sur les Tumeurs Cérébrales (ARTC). We do have a special acknowledgement for the TONIC team involved in this research project: J.-A. Lotterie, T. Duval, H. Gros-Dagnac, N. Vayssières, F. Brouillet, J.-P. Désirat, M. Calise, and D. Mélite. **Funding:** This work was supported by Recherche Innovation Thérapeutique Cancérologie (RITC REC1929), Program HTE MoGLimaging (INSERM, INCa, Plan Cancer 2016), and the Research Group of Claudius Regaud Institute (GRICR). **Author contributions:** Conceptualization: E.C.-J.M., V.L., and C.T. Design of the experiments: E.C.-J.M., C.T., C.D., and A.L.E. Coordination of the trial: E.C.-J.M. Recruitment of patients with GBM: E.C.-J.M. and V.L. Clinical data process: E.C.-J.M., M.M., and V. L. Data analysis, statistical and analytical methods supervision: T.F. and A.L.U. Process and analysis of tumor tissue samples: C.D. and A.L.E. Establishment and culture of primary cell lines: C.D., A.L.E., P.D., and F.A. Setup and process of pathological analyses on tumor samples: A.S. and Y.N. RNA-seq data analysis: J.-P.C. and M.P. Writing: A.L.E. and E.C.-J.M., with comments from all authors. **Competing interests:** E.C.-J.M. served as board expert for Novocure and received research grants from AstraZeneca, Novocure, Incyte, and Bayer. T.F. served as a consultant for Cellectis and received honoraria from Roche and Lilly. The other authors have declared that no conflict of interest exists. **Data and materials availability:** All data needed to evaluate the conclusions in the paper are present in the paper and/or the Supplementary Materials. Raw data for RNA-seq of patient biopsies have been submitted to the NCBI Gene Expression Omnibus (GEO) under accession number GSE239379. Reasonable requests for cell resources should be directed to and will be fulfilled by the corresponding authors A.L.E. and E.C.-J.M. under a material transfer agreement with Institut Claudius Regaud at IUCT–Oncopole. Notably, these requests can only concern cell lines from Sub-01 to Sub-03, due to technical constraints and low stocks for other GSC lineages.

Submitted 28 March 2023
Accepted 3 October 2023
Published 3 November 2023
10.1126/sciadv.adi0114